UNCLASSIFIED

Australian Government
Department of Defence
Science and Technology

Convex Relaxation Methods: A Review and Application to Sparse Radar Imaging of Rotating Targets

Ngoc Hung Nguyen [1], *Kutluyıl Dogancay* [1],
Paul E. Berry [2], *and Hai-Tan Tran* [2]

[1] **University of South Australia**
[2] **National Security and ISR Division**
Defence Science and Technology Group

DST-Group–RR–0444

ABSTRACT

In this report we explore the use of sparse signal representation methods in the radar imaging problem of rotating targets and compare their results. The ultimate goal is to estimate the spatial locations and corresponding reflectivities of the scatterers constituting a target, based on a signal scattered from it. We pay particular attention to the so-called convex relaxation methods, which presumably can give the sparsest possible solutions and are computationally tractable while providing provable theoretical performance guarantees. We provide a comprehensive survey on various convex relaxation problem formulations known to date, as well as known computational algorithms for solving the optimization problems. By using extensive numerical simulations with simple rotating point targets, we show that, while many of these methods perform satisfactorily for 'on-grid' cases, performance for 'off-grid' cases is mostly unsatisfactory, warranting much further research before they can be efficiently applied to the inverse problem of radar imaging.

RELEASE LIMITATION

Approved for Public Release

UNCLASSIFIED

Produced by

National Security and ISR Division
PO Box 1500
Edinburgh, South Australia 5111, Australia

Telephone: 1300 333 362

September, 2017

APPROVED FOR PUBLIC RELEASE

Convex Relaxation Methods: A Review and Application to Sparse Radar Imaging of Rotating Targets

Executive Summary

In radar imaging, sparsity and compressed sensing have been widely exploited in various problems such as sparse phase coherent imaging, wide-angle synthetic aperture radar (SAR) imaging for anisotropic scattering, multichannel SAR imaging and moving target indication, to name but a few. In this study, we focus our attention on the problem of sparsity-based radar imaging of a rotating target.

Signal analysis and radar imaging of fast-rotating objects are of particular research interest. The radar signals returned from such objects are commonly described under the general category of micro-Doppler signals which cannot be processed by conventional range-Doppler techniques and should be separated from other non-rotating scattering components prior to further processing. Specific attention is paid to rotating point-scatterer targets. The point-scatterer target model has been studied in the literature based on compressive sensing but with the restriction to the case of small angles of rotation and signals of 'moderate' bandwidths, and much less attention has been given to narrowband signals where wider angles of rotation are required.

We focus the investigation on convex relaxation methods and explore their possible applications to the radar imaging problem of a rotating target within the point-scatterer approximation, which expands on the research theme initiated in a previous report. We present a literature survey on various convex relaxation problem formulations known to date, as well as computational algorithms for solving the optimization problems and extensive numerical simulations and results. For simplicity, the current study is mostly restricted to simulated data examples where the true scatterers are 'on-grid', i.e. corresponding exactly to some of the 'atoms' in the defined dictionary. The objective is to explore how some of the best known convex relaxation methods perform when applied to the problem of estimating the spatial parameters of the scatterers, and gain insight into the performance of each relevant technique. We also find that the methods, in their current forms, do not perform satisfactorily for 'off-grid', which warrants further research.

This page is intentionally blank

Authors

Dr Ngoc Hung Nguyen
University of South Australia

Ngoc received a B.E. (Hons.) degree in electrical and electronic engineering from the University of Adelaide, Australia, in 2012 and a Ph.D. degree from University of South Australia, Australia, in 2016. Since February 2016 he has been with the Institute for Telecommunications Research, School of Information Technology & Mathematical Sciences, University of South Australia, where he is currently a research fellow. Dr Nguyen's research interests span statistical and adaptive signal processing, and its application to defence systems. His research focuses on target localization and tracking, radar waveform diversity, optimal sensor placement, and sparsity and compressive sensing for radar imaging.

Professor Kutluyil Dogancay
University of South Australia

Kutluyıl received the B.S. degree with honors in electrical and electronic engineering from Bogazici University, Istanbul, Turkey, in 1989, the M.Sc. degree in communications and signal processing from Imperial College, The University of London, U.K., in 1992, and the Ph.D. degree in telecommunications engineering from The Australian National University, Canberra, A.C.T., Australia, in 1996. Since November 1999, he has been with the School of Engineering, University of South Australia, where he is a professor and discipline leader of electrical and mechatronic engineering. His research interests span statistical and adaptive signal processing. He serves as a consultant to defence and private industry in signal processing, communications and simulation related projects. Dr. Dogancay received the Best Researcher Award of School of Engineering, University of South Australia, in 2015, and Tall Poppy Science Award of the Australian Institute of Political Science in 2005. From 2009- 2015 he was an elected member of the Signal Processing Theory and Methods (SPTM) Technical Committee of the IEEE Signal Processing Society. He is an associate member of the Sensor Array and Multichannel (SAM) Technical Committee and a member of the IEEE ComSoc Signal Processing for Communications and Electronics Technical Committee. Dr. Dogancay is the EURASIP liaison for Australia

---

Dr Paul E. Berry
National Security and ISR Division

Paul received his BSc degree with honours in 1976 from the University of London, UK and was awarded his PhD in theoretical mechanics from UCL in 1980. He works in the National Security and ISR Division of DST Group and has interests in estimation, optimisation and control applied to microwave radar engineering. He has previously worked in research laboratories in the UK's energy industry on problems of computational physics applied to power generation and transmission.

Dr Hai-Tan Tran
National Security and ISR Division

Hai-Tan graduated from the University of Sydney in 1990 and obtained his PhD degree from the Australian National University in Canberra in 1993, in the field of nonlinear guided-wave optics. He spent the next three years as a postdoctoral research fellow in the Mathematics Department of the Australian De-fence Force Academy, also in Canberra, working on the theory and simulation of spatial optical solitons and light-induced optical switching in nonlinear dielectric media, before joining the National Security and ISR Division of DST Group in 1996. His current research interests include high-resolution radar imaging, automatic target recognition, radar electronic protection, and various topics in signal processing.

Contents

Figures

1. Introduction

This report expands on the research objective in [1] exploring techniques from the area of sparse signal representations and compressive sensing for radar imaging, which is essentially an inverse problem: from a signal scattered off a target, we wish to estimate the locations and scattering amplitudes of the scatterers constituting the target. This is particularly challenging given the fact that most current methods in sparse representation are optimized based on metrics in the *time* domain of the signal, whereas target imaging relies on accurate parameter estimation in the *spatial* domain of scatterers on the target.

The current problem of interest is concerned with rotating point scatterers, which can be described as a class of micro-Doppler signals [2, 3]. In the last few years, the point scatterer model has been studied in the context of ISAR imaging based on compressive sensing [4]; however this was mostly restricted to small angles of rotation and signals of sufficient bandwidth. In applications with narrowband signals where wider angles of rotation are necessary, the research literature is still scarce.

Sparse signal representation problems have gained significant attention due to its wide range of applications ranging from engineering to the sciences. The objective of sparse representation is to approximate a received signal via a linear combination of a small number of elementary signal components drawn from a signal 'dictionary'. The sparse approximation problem is fundamentally formulated as finding the sparsest feasible solution by minimizing the l_0 norm (i.e., the number of nonzero components) of the solution. This l_0 norm minimization formulation is NP-hard in general and thus computationally intractable. Extensive research studies have been conducted over the last two decades to seek more computationally tractable methods for solving sparse approximation problems. There are five major classes available in the literature including (i) greedy pursuit, (ii) convex relaxation, (iii) Bayesian framework, (iv) nonconvex optimization, and (v) brute force [5]. Among these approaches, greedy pursuit and convex relaxation have received the most attention due to their computational tractability and provable theoretical performance guarantees. We are particularly interested in the convex relaxation methods, and explore their possible applications for radar imaging. A review of greedy pursuit techniques with the emphasis on their application to radar imaging for a rotating blade-like target can be found in [1].

2. The Radar Imaging Problem

For simplicity, the imaging problem is restricted to a two-dimensional (2D) geometry and non-interacting ideal point scatterers (Born approximation); the general 3D geometry is conceptually similar, only computationally more complex. Fig. 1 depicts a point scatterer in a 2D plane rotating with angular velocity Ω around the origin of the local coordinate system at the radial distance r and with initial angular position ψ. For a single-frequency continuous-wave (CW) transmitted signal from a monostatic radar located in the far-field of the positive y-direction, the received signal returned from the scatterer back to the radar is given by [4, 6]

$$g(t; r, \psi) = A \exp\left\{ i\frac{4\pi}{\lambda} r \sin(\Omega t + \psi) \right\} \tag{1}$$

where λ is the wavelength of the radar signal, and A represents a complex multiplicative constant corresponding to signal attenuation (assumed constant). Here, we assume that the angular velocity Ω is constant and known *a priori*.

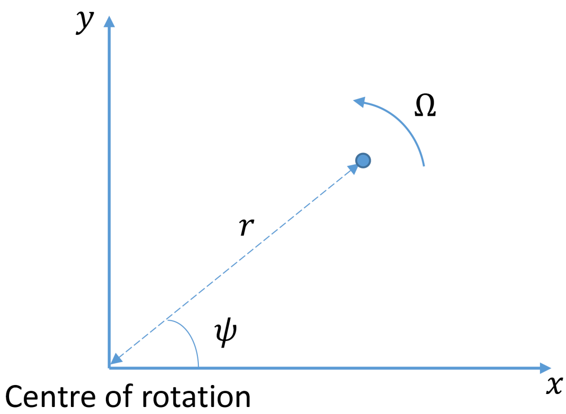

Figure 1: Geometry of a rotating point scatterer model.

When a rotating target is modelled as a rigid ensemble of K such point scatterers, the backscattered signal $s(t)$ returned from the target can be decomposed as a sum of the backscattered signals from all the scatterers:

$$s(t) = \sum_{k=1}^{K} \rho_k \, g_k(t; \boldsymbol{\vartheta}_k) + n(t) \tag{2}$$

where $g_k(t; \boldsymbol{\vartheta}_k)$ is the elementary signal component given in (1), ρ_k is the reflection coefficient, $\boldsymbol{\vartheta}_k = \{r_k, \psi_k\}$ is the spatial parameters of a scatterer, and $n(t)$ is the additive system noise. In the context of sparsity and compressive sensing, each scattering element $g_k(t; \boldsymbol{\vartheta}_k)$ is referred to as an ‘atom’. Rewriting (2) in discrete-time vector form gives

$$\mathbf{s} = \sum_{k=1}^{K} \rho_k \boldsymbol{g}_k + \boldsymbol{n} \tag{3}$$

where

$$\boldsymbol{s} = \left[s(t_1), s(t_2), \ldots, s(t_M)\right]^T \tag{4a}$$
$$\boldsymbol{g}_k = \left[g(t_1, \boldsymbol{\vartheta}_k), g(t_2, \boldsymbol{\vartheta}_k), \ldots, g(t_M, \boldsymbol{\vartheta}_k)\right]^T \tag{4b}$$
$$\boldsymbol{n} = \left[n(t_1), n(t_2), \ldots, n(t_M)\right]^T \tag{4c}$$

are vectors of M discrete-time samples of $s(t)$, $g_k(t; \boldsymbol{\vartheta}_k)$ and $n(t)$ respectively.

The choice for $\boldsymbol{\vartheta}_k$ is a design issue. In general, the chosen vectors for its components can be quite arbitrary. However, they are commonly defined as regularly spaced samples over expected ranges of values, which may happen not to coincide with the parameters of the actual scatterers of the target. When coincidence occurs, they are called ‘on-grid’; otherwise, ‘off-grid’. Furthermore, the choice of the parameter vectors, for applications in radar imaging, can be ‘dense’ in the sense that the atoms formed are mutually non-orthogonal. In this case the dictionary becomes over-complete.

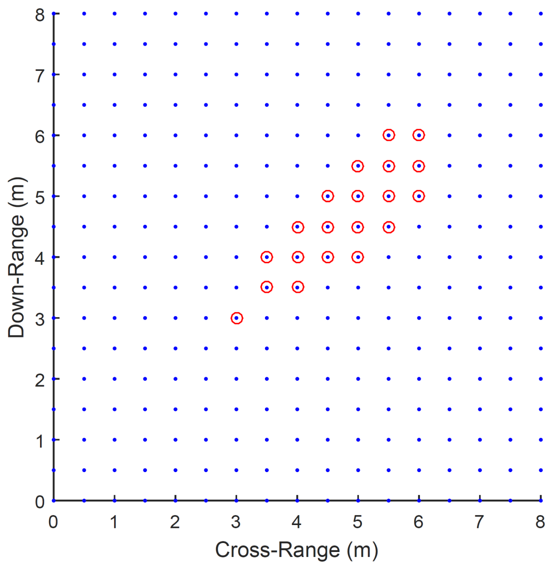

Figure 2: A example of an inverse scattering problem: a target comprising 20 *point scattering elements (labeled by red circles) and a dictionary with* 289 *point scattering atoms (labeled by blue dots) located in a regular x- and y-grid.*

Given an over-complete dictionary of N scattering atoms g_n $(n = 1, \ldots, N)$, the problem of radar imaging (i.e. inverse scattering problem) for rotating targets can be cast as a sparse approximation problem (see Fig. 2 for an example). The aim is to find a sparse solution of the linear inverse problem:

$$\boldsymbol{s} = \boldsymbol{G}\boldsymbol{\rho} + \boldsymbol{n} \tag{5}$$

where $\boldsymbol{G} = [\boldsymbol{g}_1, \boldsymbol{g}_2, \ldots, \boldsymbol{g}_N]$ is the dictionary matrix (i.e., the sensing matrix) and $\boldsymbol{\rho} = [\rho_1, \rho_2, \ldots, \rho_N]^T$ is the unknown complex coefficient vector (representing scatterer reflectivities) to be estimated.

Since a real target can often be represented by a small number of scattering elements, the coefficient vector $\boldsymbol{\rho}$ can be assumed sparse (i.e. containing a small number of nonzero elements). Note that the number of atoms in the dictionary is in general much larger than the number of signal samples (i.e., $N \gg M$), the linear system of linear equations in (5) is thus underdetermined and a unique solution cannot be determined using the conventional inverse transform of $\mathbf{G}$. However, given that the coefficient vector $\boldsymbol{\rho}$ is sparse (or can be well-approximated as being sparse), the sparsity and compressive sensing theories guarantee a stable solution for $\boldsymbol{\rho}$ [7–14].

For simplicity, the current study is mostly restricted to simulated data examples where the true scatterers are 'on-grid'. The objective of the study is to explore some of the best known convex relaxation methods applied to the problem of estimating the spatial parameters of the scatterers, and gain insight into the performance of each relevant technique. Some preliminary results on the 'off-grid' targets are also presented at the end of Section 4.

3. A Brief Survey of Convex Relaxation Methods

Consider the general linear inverse problem of

$$\boldsymbol{y} = \boldsymbol{\Phi}\boldsymbol{x} + \boldsymbol{n} \tag{6}$$

which is exactly the same form as in (5), except for the notational difference. Here, $\boldsymbol{x} \in \mathbb{C}^N$ is an unknown vector to be estimated, $\boldsymbol{y} \in \mathbb{C}^M$ is a linear measurement vector of $\boldsymbol{x}$ corrupted by an additive noise vector $\boldsymbol{n} \in \mathbb{C}^M$, and $\boldsymbol{\Phi} \in \mathbb{C}^{M\times N}$ is the dictionary whose columns have unit Euclidean norm. The sparse approximation problem is defined as [5, 13, 14]

$$\text{Find sparse } \boldsymbol{x} \text{ such that } \boldsymbol{\Phi}\boldsymbol{x} \approx \boldsymbol{y}. \tag{7}$$

The symbol $\approx$ can be defined more exactly with a chosen cost function to be minimized. Then, for each chosen cost function, several different computational algorithms may be applied for the minimization.

3.1. Sparse Approximation Problems

By 'problem', is meant 'minimization problem' characterized by a particular 'cost function'. A natural formulation for a sparse approximation problem is to find the sparsest solution of $\boldsymbol{x}$ [5, 13, 14]:

$$\min_{\boldsymbol{x}} \|\boldsymbol{x}\|_0 \quad \text{subject to} \quad \|\boldsymbol{\Phi}\boldsymbol{x} - \boldsymbol{y}\|_2 \le \epsilon \tag{8}$$

where $\|\cdot\|_0$ is the l_0 norm, which is a count of the number of nonzero components in its argument and $\epsilon > 0$ is an error tolerance. However, this l_0 *minimization* problem is NP-hard [5, 7–14], and hence is computationally intractable for practical applications [5, 7–14].

An attractive alternative approach is to replace the combinatorial l_0 function in (8) with a l_1 norm, leading to the *convex optimization* problem (or l_1 *minimization*) [5, 13, 14]:

$$(\mathrm{BP}_\epsilon) \qquad \min_{\boldsymbol{x}} \|\boldsymbol{x}\|_1 \quad \text{subject to} \quad \|\boldsymbol{\Phi}\boldsymbol{x} - \boldsymbol{y}\|_2 \le \epsilon \tag{9}$$

where $\|\boldsymbol{x}\|_1 = \sum_i |\boldsymbol{x}_i|$ denotes the l_1 norm of the vector $\boldsymbol{x}$. Since the l_1 norm is the convex function closest to the l_0 quasi-norm, this replacement is commonly referred to as *convex relaxation* [5, 13, 14]. The convex relaxation approach has been demonstrated in the literature to result in optimal or near-optimal solution to sparse approximation problems in various settings (see e.g., [12, 15–23] and the references therein).

In addition to the quadratically constrained l_1 minimization formulation in (9), there exists an *unconstrained* l_1 *regularization* formulation which has also received much attention in the literature [5, 13, 14]:

$$(\mathrm{QP}_\kappa) \qquad \min_{\boldsymbol{x}} \left\{ \frac{1}{2}\|\boldsymbol{\Phi}\boldsymbol{x} - \boldsymbol{y}\|_2^2 + \kappa\|\boldsymbol{x}\|_1 \right\} \tag{10}$$

which is commonly known as the basis pursuit denoising (BPDN) criterion [24]. In fact, the use of l_1 regularization has a long history as outlined in [12]. Here, $\kappa > 0$ is a regularization parameter which governs the tradeoff between the sparsity of the solution and the approximation error. In particular, larger values of κ typically lead to sparser solutions of $\boldsymbol{x}$.

The third formulation is the *least absolute shrinkage and selection operator (LASSO)* [5, 13, 14, 25]:

$$(\mathrm{LS}_\tau) \quad \min_{\boldsymbol{x}} \|\boldsymbol{\Phi x} - \mathbf{y}\|_2^2 \quad \text{subject to} \quad \|\boldsymbol{x}\|_1 \leq \tau. \tag{11}$$

It is asserted from the standard optimization theory [26] that the three formulations (BP_ϵ), (QP_κ) and (LS_τ) are equivalent for appropriate choices of ϵ, κ and τ. Unfortunately, except for the special case where the dictionary matrix $\boldsymbol{\Phi}$ is orthogonal, the conditions of ϵ, κ and τ yielding the equivalence between (BP_ϵ), (QP_κ) and (LS_τ) are generally difficult to compute [27, 28]. In many applications, a reasonable estimate of ϵ can be obtained from the noise level of measurements, thereby making (BP_ϵ) preferable. A common choice for ϵ is $\epsilon = \sigma\sqrt{M + 2\sqrt{2M}}$ where σ is the noise power level. However, the constrained problem (BP_ϵ) is in general more difficult to solve than the unconstrained problem (QP_κ) which has close connection with convex quadratic programming. In contrast to ϵ, it is more difficult to select an appropriate value for κ since the link between κ and σ is less clear. It is argued in [24] that the choice of $\kappa = \sigma\sqrt{2\log N}$ provides important optimality properties. However, this argument is restricted to the case where the dictionary matrix $\boldsymbol{\Phi}$ is orthogonal. Therefore, (QP_κ) may need to be solved repeatedly for various values of κ or to systematically find the path of the solutions as κ decreases toward zero [5].

In addition to the l_1 norm formulations in (9)–(11), *total-variation (TV) regularization* is also commonly used in the literature of sparsity and compressed sensing [28–31]:

$$\min_{\boldsymbol{x}} \left\{ \frac{1}{2}\|\boldsymbol{\Phi x} - \boldsymbol{y}\|_2^2 + \nu\|\boldsymbol{x}\|_{\mathrm{TV}} \right\} \tag{12}$$

where $\|\boldsymbol{x}\|_{\mathrm{TV}} = \|D\{|\boldsymbol{x}|\}\|_1$ with D denoting a discrete approximation to the derivative (gradient) operator. In fact, if $\boldsymbol{x}$ is a piecewise constant object, then the TV regularization in (12) will provide more accurate recovery [28]. Specifically, the l_1 norm formulations tend to reduce extended objects into points or miss small target features in this case. On the other hand, the TV regularizer in (12) promotes solutions which are clustered and not fragmented, thus leading to a more smooth image representation of the target. The l_1 regularization and TV regularization can be combined and used in parallel as [31]

$$\min_{\boldsymbol{x}} \left\{ \frac{1}{2}\|\boldsymbol{\Phi x} - \boldsymbol{y}\|_2^2 + \kappa \sum_i \left(|\boldsymbol{x}_i|^2 + \delta\right)^{1/2} + \nu \sum_i \left(|D_i\{|\boldsymbol{x}|\}|^2 + \delta\right)^{1/2} \right\} \tag{13}$$

where the second and third terms are the smooth approximations of the l_1 norm and the TV norms, respectively, with a small constant $\delta \geq 0$.

Each of the above problems may be solved by a number of different computational algorithms, as summarized in Section 3.2.

3.2. Computational Algorithms

3.2.1. Interior-Point Algorithms

Interior-point based methods were one of very first approaches proposed in the literature for solving sparse approximation problems via convex relaxation. The techniques described in this section assume variables are real and their extension to complex variables is discussed in Section 4. In [24], the problem (QP_κ) is reformulated as a perturbed linear program which, in the case of real variables, can be solved based on the primal-dual interior point framework. In particular, the problem (QP_κ) is equivalent to

$$\min_{\boldsymbol{u},\boldsymbol{v}} \left\{ \frac{1}{2}\|\boldsymbol{y} - \boldsymbol{\Phi}(\boldsymbol{u}-\boldsymbol{v})\|_2^2 + \kappa \mathbf{1}^T\boldsymbol{u} + \kappa \mathbf{1}^T\boldsymbol{v} \right\} \quad \text{subject to} \quad \boldsymbol{u},\boldsymbol{v} \geq \mathbf{0} \tag{14}$$

by defining $\boldsymbol{x} \equiv \boldsymbol{u} - \boldsymbol{v}$ (i.e., indeed $\boldsymbol{\Phi x} = \boldsymbol{\Phi}(\boldsymbol{u}-\boldsymbol{v})$ and $\mathbf{1}^T\boldsymbol{u} + \mathbf{1}^T\boldsymbol{v} = \|\boldsymbol{x}\|_1$). Here the notation $\mathbf{1} \in \mathbb{R}^N$ denotes the all-ones vector. By using the translation of $\boldsymbol{z} \Leftrightarrow [\boldsymbol{u}^T, \boldsymbol{v}^T]^T$, $\boldsymbol{c} \Leftrightarrow \kappa[\mathbf{1}^T, \mathbf{1}^T]^T$, $\boldsymbol{A} \Leftrightarrow [\boldsymbol{\Phi}, -\boldsymbol{\Phi}]$ and $\boldsymbol{b} \Leftrightarrow \boldsymbol{s}$, (14) becomes

$$\min_{\boldsymbol{z}} \left\{ \frac{1}{2}\|\boldsymbol{Az} - \boldsymbol{b}\|_2^2 + \boldsymbol{c}^T\boldsymbol{z} \right\} \quad \text{subject to} \quad \boldsymbol{z} \geq \mathbf{0} \tag{15}$$

which is a least squares problem with positivity constraints. In fact, this least squares problem is equivalent to a perturbed linear program:

$$\min_{\boldsymbol{z},\boldsymbol{p}} \left\{ \boldsymbol{c}^T\boldsymbol{z} + \frac{1}{2}\|\boldsymbol{p}\|^2 \right\} \quad \text{subject to} \quad \boldsymbol{Az} + \delta\boldsymbol{p} = \boldsymbol{b},\ \boldsymbol{x} \geq \mathbf{0},\ \delta = 1. \tag{16}$$

To solve (16), the authors in [24] exploited the use of the primal-dual log-barrier method which aims to solve a more general perturbed linear program:

$$\min_{\boldsymbol{z},\boldsymbol{p}} \left\{ \boldsymbol{c}^T\boldsymbol{z} + \frac{1}{2}\|\gamma\boldsymbol{z}\|^2 + \frac{1}{2}\|\boldsymbol{p}\|^2 \right\} \quad \text{subject to} \quad \boldsymbol{Az} + \delta\boldsymbol{p} = \boldsymbol{b},\ \boldsymbol{x} \geq \mathbf{0}. \tag{17}$$

where γ and δ are perturbation parameters (normally small, e.g., 10^{-4}). By setting $\delta = 1$, this will solve the problem (QP_κ). Further details on the primal-dual interior-point algorithm can be found in [24, 32, 33].

In contrast to [24], the work in [34] transformed the problem (QP_κ), again for real variables, into a convex quadratic problem with linear inequality constraints of

$$\min_{\boldsymbol{x},\boldsymbol{u}} \left\{ \frac{1}{2}\|\boldsymbol{\Phi x} - \boldsymbol{y}\|_2^2 + \kappa \sum_{i=1}^{N} u_i \right\} \quad \text{subject to} \quad -u_i \leq x_i \leq u_i\,(i = 1, \ldots, N) \tag{18}$$

which is then solved using a primal log-barrier method. Here, x_i and u_i ($i = 1, \ldots, N$) are the entries of $\boldsymbol{x}$ and $\boldsymbol{u}$ respectively. In particular, the primal log-barrier method proposed in [34] relies on a preconditioned conjugate gradients (PCG) algorithm to compute the search direction for interior-point computations. Note that the method in [24] makes use of the LSQR algorithm without preconditioning to compute the search direction. In addition, the method in [34] also incorporates a truncation rule to determine the search direction that provides a good trade-off between computational cost and convergence rate.

Another interior-point based algorithm for convex relaxation with real variables was presented in [35] which recast the problem (BP_ϵ) as second-order cone programs (SOCPs) and applies the generic log-barrier algorithm described in [36] to obtain the solution. Specifically, the problem (BP_ϵ) can rewritten as

$$\begin{aligned} \min_{\boldsymbol{x},\boldsymbol{u}} \sum_{i=1}^{N} u_i \quad \text{subject to} \quad & -u_i \leq x_i \leq u_i\,(i = 1, \ldots, N), \\ & \frac{1}{2}\left(\|\boldsymbol{\Phi x} - \boldsymbol{y}\|_2^2 - \epsilon^2\right) \leq 0. \end{aligned} \tag{19}$$

3.2.2. Gradient Algorithms

Gradient-descent based methods are first-order iterative algorithms for solving the problem (QP_κ) by iteratively computing the next iterate $\boldsymbol{x}_{t+1}$ ($t = 1, 2, \dots$) based on the gradient of the least squares term obtained at the current iterate $\boldsymbol{x}_t$ (viz., $\boldsymbol{\Phi}^T(\boldsymbol{\Phi}\boldsymbol{x}_t - \boldsymbol{y})$):

$$\boldsymbol{x}_t^+ := \arg\min_{\boldsymbol{z}} \left\{ (\boldsymbol{z} - \boldsymbol{x}_t)^T \boldsymbol{\Phi}^T(\boldsymbol{\Phi}\boldsymbol{x}_t - \boldsymbol{y}) + \frac{1}{2}\alpha_t \|\boldsymbol{z} - \boldsymbol{x}_t\|_2^2 + \kappa\|\boldsymbol{z}\|_1 \right\} \tag{20a}$$

$$\boldsymbol{x}_{t+1} := \boldsymbol{x}_t + \gamma_t(\boldsymbol{x}_t^+ - \boldsymbol{x}_t) \tag{20b}$$

for given choice of scalar parameters α_t and γ_t. An equivalent form of subproblem (20a) is

$$\boldsymbol{x}_t^+ := \arg\min_{\boldsymbol{z}} \left\{ \frac{1}{2} \left\| \boldsymbol{z} - \left(\boldsymbol{x}_t - \frac{1}{\alpha_t}\boldsymbol{\Phi}^T(\boldsymbol{\Phi}\boldsymbol{x}_t - \boldsymbol{y}) \right) \right\|_2^2 + \frac{\kappa}{\alpha_t}\|\boldsymbol{z}\|_1 \right\}. \tag{21}$$

This approach is commonly known in the literature as iterative shrinkage/thresholding (IST) methods. A number of algorithms in this family have been develped in the literature including the forward-backward splitting algorithm [37], the fixed-point continuation (FPC) algorithm [38], the thresholded Landweber algorithm [39], the iterative denoising algorithm [40], and the sparse reconstruction via separable approximation (SpaRSA) algorithm [30]. The IST methods in general exhibits slow convergence in practice as the standard convergence results for these techniques require that $\inf_t \alpha_t > \|\boldsymbol{\Phi}^T\boldsymbol{\Phi}\|_2/2$ [37]. However, the SpaRSA approach in [30] leads to more practical IST variants which allow smaller values of α_t given that the objective function in (10) decreases sufficiently over a span of successive iterations. In particular, in contrast to other IST methods which rely on a more conservative selection of α_t based on the Lipschitz constant of the gradient, the SpaRSA algorithm exploits the use of Barzilai-Borwein formulas to select the value of α_t within the spectrum of $\boldsymbol{\Phi}^T\boldsymbol{\Phi}$. Therefore, the SpaRSA algorithm can be considered as an accelerated IST version with a better practical performance as a benefit of variation of α_t.

Another accelerated variant of IST was proposed in [29], namely the two-step IST (TwIST) method. The objective of the TwIST method is to merge the performance advantage of the IST scheme and the capability to handle ill-posed problems of the re-weighted shrinkage scheme. In particular, the two-step iteration of TwIST is given by

$$\boldsymbol{x}_{t+1} = (1 - \alpha)\boldsymbol{x}_{t-1} + (\alpha - \beta)\boldsymbol{x}_t + \beta\boldsymbol{x}_t^+ \tag{22}$$

with the initialization of $\boldsymbol{x}_1 = \boldsymbol{x}_0^+$. The main difference of the TwIST method over the original IST methods is that it also incorporates the previous iterate $\boldsymbol{x}_{t-1}$ to compute $\boldsymbol{x}_{t+1}$. Importantly, it was shown in [29] that TwIST converges significantly faster than the original IST. In addition to TwiST, [41] presents a different IST variant, viz. the fast iterative shrinkage-thresholding algorithm (FISTA) based on optimal gradient methods for convex minimization proposed by Nesterov in [42]. The utilization of optimal gradient methods to sparse approximation can also be found in [28], leading to the development of the NESTA algorithm. However, it should be noted that the NESTA algorithm aims to solve the problem (BP_ϵ) instead of the problem (QP_κ) as in [41].

The fixed-point continuation and active set (FCP-AC) method [43] is a successor of the FPC method [38]. The motivation behind FCP-AC is to combine the performance advantages of both greedy algorithms and convex relaxation algorithms. In particular, each iteration of the FPC-AC method consists of two stages. The first stage performs the first-order method, i.e., shrinkage iterations, as used in the FPC method to determine the active index set corresponding to the nonzero elements of the current iterate of the solution. The second stage utilizes the second-order method to solve a smooth subspace optimization associated with the active index set. Note that the FPC method incorporates a debiasing step to refine the final solution, which is similar to the second stage of the FPC-AC method. However, the debiasing procedure (see below for further discussion) is only performed once as a post-processing step at the end of the FPC algorithm, while the subspace optimization is integrated into the main iterations of the FPC-AC algorithm.

Another gradient-based method for l_1-regularization, viz. the gradient projection for sparse reconstruction (GPSR) method, was proposed in [44]. The main idea behinds GPSR is to re-express the problem (QPκ) as a convex quadratic program by splitting the variable $\boldsymbol{x}$ into positive and negative parts. Explicitly, we have

$$\boldsymbol{x} = \boldsymbol{u} - \boldsymbol{v},\ \boldsymbol{u} \geq \boldsymbol{0},\ \boldsymbol{v} \geq \boldsymbol{0}. \tag{23}$$

where $u_i = (x_i)_+$ and $v_i = (-x_i)_+$ for all $i = 1, 2 \ldots, N$. Here, $(x)_+ = \max\{0, x\}$ is the positive-part operator. As a result, the problem (QP$_\kappa$) in (10) can be reformulated into the bound-constrained quadratic program (BCQP) as in (14). To solve this BCQP, the authors in [44] rewrite (14) in a more standard BCQP form:

$$\min_{\boldsymbol{z}} \left\{ \boldsymbol{c}^T \boldsymbol{z} + \frac{1}{2} \boldsymbol{z}^T \boldsymbol{B} \boldsymbol{z} \right\} \quad \text{subject to} \quad \boldsymbol{z} \geq \boldsymbol{0} \tag{24}$$

where

$$\boldsymbol{z} = \begin{bmatrix} \boldsymbol{u} \\ \boldsymbol{v} \end{bmatrix},\ \boldsymbol{b} = \boldsymbol{\Phi}^T \boldsymbol{y},\ \boldsymbol{c} = \kappa \mathbf{1}_{2N\times 1} + \begin{bmatrix} -\boldsymbol{b} \\ \boldsymbol{b} \end{bmatrix}, \tag{25}$$

and

$$\boldsymbol{B} = \begin{bmatrix} \boldsymbol{A}^T\boldsymbol{A} & -\boldsymbol{A}^T\boldsymbol{A} \\ -\boldsymbol{A}^T\boldsymbol{A} & \boldsymbol{A}^T\boldsymbol{A} \end{bmatrix}, \tag{26}$$

and we apply the following gradient projection iteration to obtain the solution:

$$\boldsymbol{w}_t = \Big(\boldsymbol{z}_t - \alpha_t \nabla F(\boldsymbol{z}_t) \Big)_+ \tag{27a}$$

$$\boldsymbol{z}_{t+1} = \boldsymbol{z}_t + \gamma_t (\boldsymbol{w}_t - \boldsymbol{z}_t) \tag{27b}$$

for some chosen scalar parameters α_t and γ_t. Here, $F(\boldsymbol{z}) \equiv \boldsymbol{c}^T\boldsymbol{z} + \frac{1}{2}\boldsymbol{z}^T\boldsymbol{B}\boldsymbol{z}$. Two versions of GPSR, namely GPSR-Basic and GPSR-BB, were proposed in [44] with different choices of α_t and γ_t. In particular, the GPSR-BB algorithm relies on the Barzilai-Borwein approach for parameter selection.

In addition to the aforementioned gradient-descent methods, the spectral projected-gradient (SPG) method [45] was also exploited in [27] to solve the problem (LS$_\tau$). Basically, the SPG method computes the solution iteratively using the rule

$$\boldsymbol{x}_{t+1} = P_\tau \{ \boldsymbol{x}_t - \alpha_t g(\boldsymbol{x}_t) \} \tag{28}$$

and utilizes Barzilai-Borwein formulas for selecting the step size α_t. Here, $P_\tau\{\cdot\}$ is the orthogonal projection operator of an $N \times 1$ vector onto the convex set $\|\boldsymbol{x}\|_1 \leq \tau$, i.e.,

$$P_\tau\{\boldsymbol{c}\} = \arg\min_{\boldsymbol{x}} \|\boldsymbol{c} - \boldsymbol{x}\|_2 \quad \text{subject to} \quad \|\boldsymbol{x}\|_1 \leq \tau, \tag{29}$$

and $g(\boldsymbol{x}_t)$ is the gradient of $\|\boldsymbol{\Phi}\boldsymbol{x} - \boldsymbol{y}\|_2^2$ computed at the current iterate $\boldsymbol{x}_t$.

Similarly to the regularization parameter κ in the problem (QPκ), it is difficult to choose an appropriate value for the constraint parameter τ in the problem (LS$_\tau$) unless prior knowledge of the unknown $\boldsymbol{x}$ is available. Inspired by the fact that the formulation (BP$_\epsilon$) is preferred in many applications where the parameter ϵ can be estimated from prior information on noise levels, the authors in [27] have developed a root finding procedure that identifies the value of τ for which the solution of (LS$_\tau$) coincides with the solution of (BP$_\epsilon$) for a given value of ϵ. Given $\boldsymbol{x}_\tau$ is the optimal solution of (LS$_\tau$), the main idea of the root-finding algorithm proposed in [27] is to apply Newton's method to find a root of the nonlinear equation

$$\phi(\tau) = \epsilon \quad \text{with} \quad \phi(\tau) = \|\boldsymbol{\Phi}\boldsymbol{x}_\tau - \boldsymbol{y}\|_2, \tag{30}$$

which defines a sequence of τ_k that approaches τ_ϵ, where $\boldsymbol{x}_{\tau_\epsilon}$ is the solution of (BP$_\epsilon$). Specifically, this root-finding algorithm exploits the use of the Pareto curve that defines the optimal trade-off between $\|\boldsymbol{\Phi}\boldsymbol{x} - \boldsymbol{y}\|_2$ and $\|\boldsymbol{x}\|_1$. Here, the function ϕ is used to parameterize the Pareto curve in terms of τ. Since the function ϕ and thus the Pareto curve are continuously differentiable, Newton's method can be applied to find roots of the nonlinear equation (30) which correspond to points on the Pareto curve.

Note that some of the algorithms mentioned above (e.g., TwiST, FISTA and SpaRSA) in fact can be used to solve a more general form of the l_1 regularization problem:

$$\min_{\boldsymbol{x}} \left\{ \frac{1}{2} \|\boldsymbol{\Phi}\boldsymbol{x} - \boldsymbol{y}\|_2^2 + \kappa f(\boldsymbol{x}) \right\} \tag{31}$$

where $f(\boldsymbol{x})$ is the general regularization function. Therefore, these algorithms can be applied to solve the TV regularization formulation as well as the mixed l_1 and TV regularization formulation.

3.2.3. Warm Starting and Adaptive Continuation

Warm starting is motivated by the fact that the gradient-based methods in general benefit significantly from a good initial point $\boldsymbol{x}_0$ [30, 44]. The main idea is to use the solution of (10) for a given value of κ to initialize the gradient-based methods in solving (10) for a nearby value of κ. In general, fewer iterations are required for the next "warm-started" run. As a result, one can effectively solve (10) for a sequence of values of κ using this warm-start strategy.

As mentioned above, from a practical point of view, it is difficult to select an appropriate value for the regularization parameter for the problem (QP$_\kappa$) in (10). Therefore, one may wish to solve (10) repeatedly for a range of values of κ and apply some tests by means of the solution sparsity and/or the least-squares fit to determine the "best" solution among the obtained solutions. This is the second motivation for the use of warm starting.

Another important application of the warm-start technique is continuation [28, 30, 38, 43, 44] in which the problem (QP$_\kappa$) in (10) is solved for decreasing sequence of values of κ. The chief motivation for using a decreasing sequence of κ values is that it has been observed in [28, 30, 38, 43, 44] that solving the problem (QP$_\kappa$) becomes slow for small values of κ. As a result, the problem (QP$_\kappa$) can be solved more effectively by starting with a larger value of κ and decreasing κ in steps to its desired value. Since, the unique solution to the problem (QP$_\kappa$) is the zero vector for $\kappa \geq \|\boldsymbol{\Phi}^T \boldsymbol{y}\|_\infty$ ($\|\boldsymbol{w}\|_\infty = \max_i \|w_i\|$ with w_i being the entries of $\boldsymbol{w}$) [34], $\kappa \lesssim \|\boldsymbol{\Phi}^T \boldsymbol{y}\|_\infty$ can be considered as "large" while $\kappa \ll \|\boldsymbol{\Phi}^T \boldsymbol{y}\|_\infty$ can be considered as "small". Inspired by this fact, an adaptive continuation scheme was proposed in [30] as summarized in Algorithm 1.

Algorithm 1 Adaptive Continuation

Initialisation: $t \leftarrow 0$, $\boldsymbol{x}_t \leftarrow \boldsymbol{x}_0$
$\boldsymbol{y}_t \leftarrow \boldsymbol{y}$
repeat
$\kappa_t \leftarrow \max\{\zeta \|\boldsymbol{\Phi}^T \boldsymbol{y}_t\|_\infty, \kappa\}$, where $\zeta < 1$
$\boldsymbol{x}_{t+1} \leftarrow$ solution of (QP$_\kappa$) for inputs $\boldsymbol{y}$ and $\boldsymbol{\Phi}$ with parameter $\kappa = \kappa_t$ and initialized at $\boldsymbol{x}_t$
$\boldsymbol{y}_{t+1} \leftarrow \boldsymbol{y} - \boldsymbol{\Phi}\boldsymbol{x}_{t+1}$
$t \leftarrow t + 1$
until $\kappa_t = \kappa$

It is noted that the continuation is originally inspired by the homotopy technique [46, 47] which solves the LASSO problem (LS$_\tau$). Fundamentally, the homotopy methods exploit the piecewise linear property of the solution as a function of the constraint parameter τ to generate a full path of solutions for a range of values of τ. Specifically, these methods start with $\tau = 0$ (i.e., the corresponding solution is $\boldsymbol{x} = \boldsymbol{0}$) and progressively find the next turning point (i.e., the next largest value of τ) at which one component of $\boldsymbol{x}$ switches from nonzero to zero or vice versa. Each iteration of the homotopy methods require a least-squares estimation over the column submatrix of $\boldsymbol{\Phi}$ corresponding to the nonzero component of the current iterate of $\boldsymbol{x}$.

3.2.4. Debiasing/Reweighting

Debiasing was introduced for several convex relaxation methods (see e.g., [30, 44]) aiming to eliminate the signal attenuation due to the presence of the regularization term. Debiasing is basically a post-processing step to minimize the least-squares objective $\|\boldsymbol{\Phi}\boldsymbol{x} - \boldsymbol{y}\|_2^2$ over the nonzero elements of the solution obtained from a given convex relaxation algorithm:

$$\min_{\boldsymbol{x}_\mathcal{I}} \|\boldsymbol{\Phi}_\mathcal{I} \boldsymbol{x}_\mathcal{I} - \boldsymbol{y}\|_2^2 \tag{32}$$

where $\mathcal{I}$ is the set of indices corresponding to nonzero elements in the obtained solution, $\boldsymbol{\Phi}_\mathcal{I}$ is the column submatrix of $\boldsymbol{\Phi}$ corresponding to $\mathcal{I}$, and $\boldsymbol{x}_\mathcal{I}$ is the subvector of $\boldsymbol{x}$ corresponding to $\mathcal{I}$. In other words, debiasing is a reweighting procedure over the set of nonzero elements of the obtained solution $\hat{\boldsymbol{x}}$ according to the least-squares criterion.

In the following (Section 4.1.5) the debiasing/reweighting idea is extended into a more general context of "significant" elements. In particular, the debiasing/reweighting procedure is performed over a set of significant elements in the obtained solution. An element is considered significant either if it belongs to a group of largest elements or if it is larger than a certain threshold. Other insignificant elements are set to zero after the debiasing/reweighting scheme.

4. Simulations and Discussion

We now present and discuss numerical simulations to demonstrate the performance of the convex relaxation methods described in the previous Section. The signals are from rigidly rotating point scatterers described in Section 2.

4.1. Methods Involving Only the l_1 Norm

4.1.1. Simulation Setup

Consider a synthetic two-dimensional radar imaging scenario where a single-frequency CW monostatic radar illuminates a rotating target. The target rotates around the origin of the target local coordinate at 40 rad/sec. The target is modelled as a set of point scatterers specified by their reflectivity (i.e., characterized by the coefficients ρ_k in (2)) and their locations (i.e., characterized by the radial distance r_k and the angular position ψ_k). The radar is located in the far-field of the positive y-direction of the target coordinate operating at the frequency of 9.5 GHz and the sampling rate of 66 kHz. For this simulation, the target model consists of 10 groups of points, each group is made of 4 on-grid points placed around a square shape of various spacings and radial distance from the centre of rotation, as depicted in Fig. 3. The signal to noise ratio (SNR) is set to 10 dB. The received signal model in (2) is used to generate the simulated data in one rotation cycle of the target. Fig. 4 plots the magnitudes of the simulated original signal and the magnitude of one realization of the simulated noise-corrupted signals in the time domain.

A point-scatterer dictionary is constructed using (1) from a regular grid of atom locations in the Cartesian coordinate, viz., $x \in \{-50\Delta x : \Delta x : 50\Delta x\}$ and $y \in \{0 : \Delta y : 50\Delta y\}$. Here, $\Delta x = \Delta y = \lambda/2$ are the grid step sizes, where λ denotes the radar signal wavelength.

It is also noted that some of the methods cannot handle complex-valued signal directly. Therefore, the real and imaginary parts of the radar signal are decoupled and concatenated together to form a new real-valued signal, and the dictionary is decoupled into real and imaginary submatrices to create a new real-valued dictionary matrix as in [48–51]. This conversion has been used widely in the literature for many radar imaging applications (see, e.g., [48–51]), and is performed here as a pre-processing step in our simulation.

4.1.2. Results for l_1 Minimization

We apply the SPG method [27] to obtain the solutions of the l_1 minimization formulation with various values of ϵ, i.e., the constraint parameter on the l_2 norm of the residual. For the sake of convenience, the l_1 minimization formulation in (9) is given again here:

$$(\text{BP}_\epsilon) \quad \min_{\boldsymbol{x}} \|\boldsymbol{x}\|_1 \quad \text{subject to} \quad \|\boldsymbol{\Phi x} - \boldsymbol{y}\|_2 \le \epsilon.$$

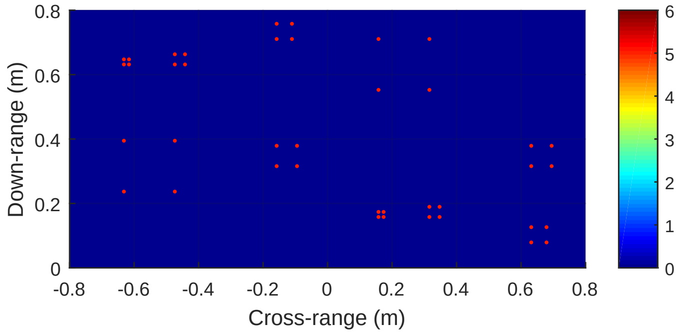

Figure 3: Simulated target with 8 *square components with each consisting of* 4 *point scatterers at the corners.*

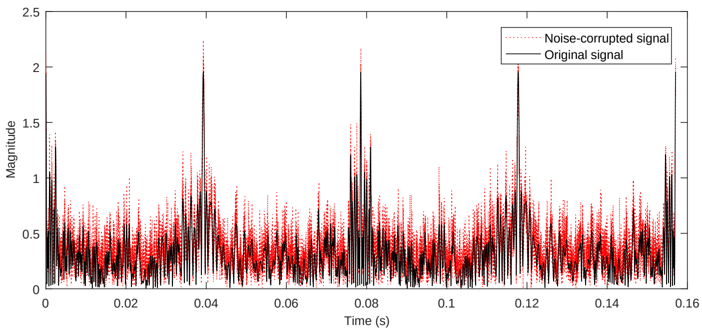

Figure 4: Simulated backscattered signal from the target depicted in Fig. 3 versus time.

Fig. 5 shows the normalized l_2 norm of the residual, the normalized l_1 norm of the solution and the running time against $f_\epsilon = \epsilon/\sigma \in \{0.701, 0.801, 0.901, 1.001, 1.101, 1.201, 1.301\}$ (where σ is the noise level). Note that the l_2 norm of the residual is normalized by the noise level σ and the l_1 norm of the solution is normalized by the l_1 norm of the ground-truth solution. Note also that the results in Fig. 5 are obtained by averaging via 10 Monte Carlo (MC) simulation runs. It is observed that, for $\epsilon > \sigma$, the l_2 norm of the residual of the solution agrees with the corresponding constraint parameter value ϵ. On the other hand, the SGP method fails to converge for $\epsilon < \sigma$ and thus cannot achieve the desired values for the l_2 norm of the residual. In addition, we can observe the trade-off between the signal reconstruction error (i.e., the l_2 norm of the residual) and the sparsity of the solution (i.e., the l_1 norm of the solution). Specifically, the l_1 norm of the solution increases as ϵ decreases. The l_1 norm of the solution approaches the l_1 norm of the ground-truth solution as ϵ approaches the noise level σ. It is also observed that the SPG method takes longer to compute the solution for smaller value of ϵ as expected. In particular, the running time for $\epsilon < \sigma$ is significantly larger than for $\epsilon > \sigma$ since the SPG algorithm in this case only stops when the maximum number of allowed iteration (viz., 150 iterations) is reached.

Fig. 6 shows the reconstructed signal obtained in the first MC run in the time domain from 0.02 sec to 0.06 sec for each value of ϵ. It is observed that the reconstructed signal gets closer to the original signal as ϵ decreases. In particular, an almost perfect reconstruction is obtained for $f_\epsilon = 1.001, 0.901, 0.801$ and 0.0701. However, good time-domain signal reconstruction

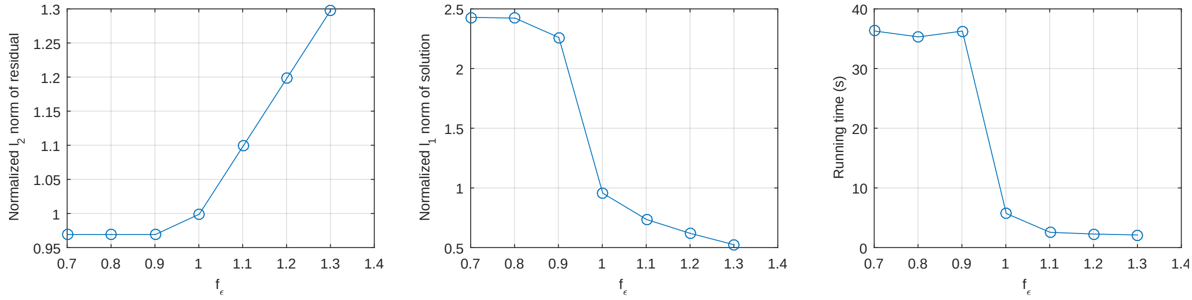

Figure 5: Results for the l_1 minimization formulation: the normalized l_2 norm of the residual, the l_1 norm of the solution and the running time against $f_\epsilon = \epsilon/\sigma$.

does not always lead to good reconstruction in terms of scatterer imaging as shown in Fig. 7 which shows the corresponding reconstructed scatterer image of the target in comparison with the ground-truth scatterer image. For too large values of ϵ, i.e., $f_\epsilon = 1.301, 1.201$ and 1.101, correct scatterers are identified but with much lower coefficients than the ground truth. In contrast, for too small values of ϵ, i.e., $f_\epsilon = 0.901, 0.801$ and 0.701, other false-alarm scatterers appear and consequently affect the coefficients of the correct scatterers even though the time-domain signal is almost perfectly reconstructed with these values of ϵ. For $f_\epsilon = 1.001$, i.e., the constraint parameter ϵ is set to a value slightly larger than the noise level σ, we obtain good reconstruction both in time-domain representation as well as in scatterer imaging representation. The considered imaging problem can be viewed intuitively as a target and noise separation problem. With an appropriate value of the constraint ϵ for the signal residual (i.e., around the noise level), the noise is well separated from the target, leading to a very nice and clean reconstructed scatterer image as shown in Fig. 7(e). For too small value of ϵ, a part of target signal is perceived as noise, and thus leading to weaker scatterers as shown in Figs. 7(b)–(d). In constrast, for too large value of of ϵ, a part of noise is now perceived as target, thus leading to the presence of false-alarm scatterers as shown in Figs. 7(f)–(h).

4.1.3. Results for l_1 Regularization

We now investigate the performance of the l_1 regularization formulation (QP$_\kappa$) for various values of the regularization parameter κ. For the sake of convenience, we recall the formula for l_1 regularization given in Section 3:

$$(\mathrm{QP}_\kappa) \qquad \min_{\boldsymbol{x}} \left\{ \frac{1}{2} \|\boldsymbol{\Phi x} - \boldsymbol{y}\|_2^2 + \kappa \|\boldsymbol{x}\|_1 \right\}.$$

The GPSR-BB algorithm [44] is used to obtain the solution for the problem (QP$_\kappa$). Fig. 8 plots the normalized l_2 norm of the residual, the normalized l_1 norm of the solution and the running time averaged via 10 MC runs against $f_\kappa = \kappa/\|\boldsymbol{\Phi}^T \boldsymbol{y}\|_\infty \in \{0.001, 0.005, 0.01, 0.05, 0.1, 0.5, 0.9\}$. Similar to the results presented in Section 4.1.2, we also observe the trade-off between the the signal reconstruction error and the sparsity of the solution. In particular, the l_2 norm of the residual increases while the l_1 norm of the solution decreases as κ increases. Moreover, it is also seen from Fig. 8 that solving (QP$_\kappa$) becomes slower for smaller values of κ.

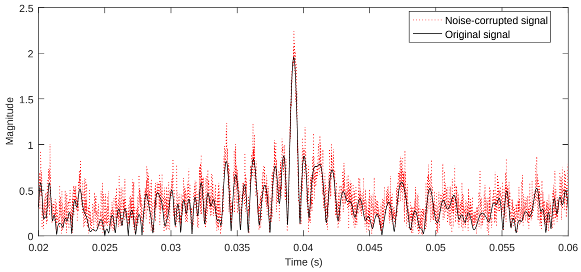

(a) Noise-corrupted signal

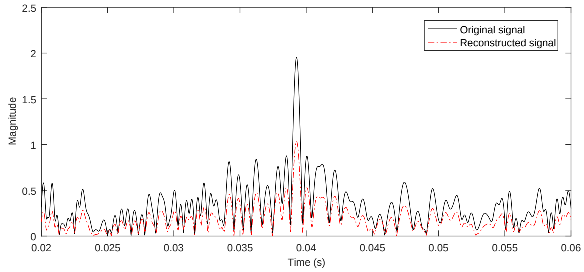

(b) Reconstructed signal ($f_\epsilon = 1.301$)

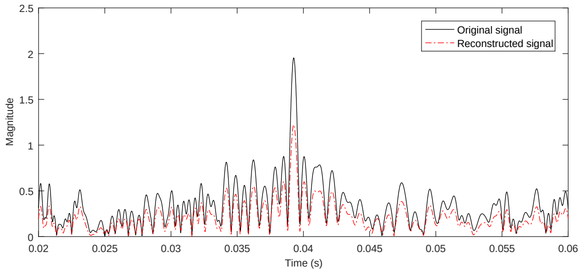

(c) Reconstructed signal ($f_\epsilon = 1.201$)

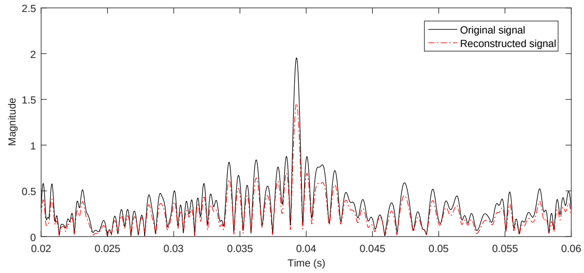

(d) Reconstructed signal ($f_\epsilon = 1.101$)

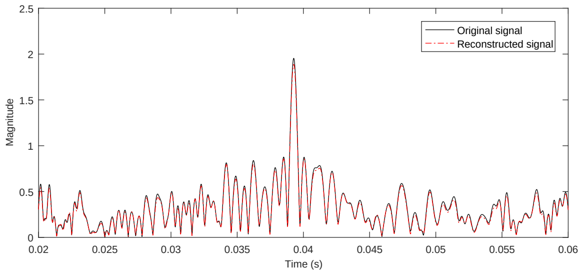

(e) Reconstructed signal ($f_\epsilon = 1.001$)

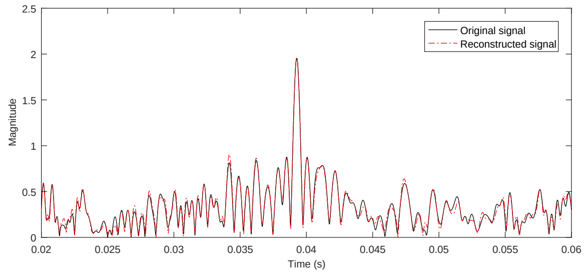

(f) Reconstructed signal ($f_\epsilon = 0.901$)

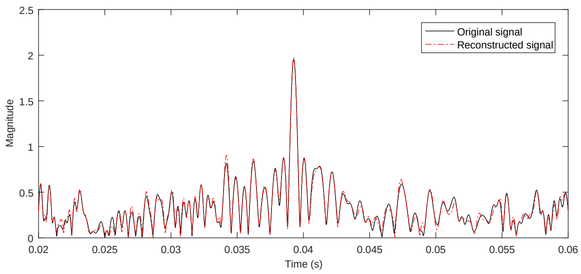

(g) Reconstructed signal ($f_\epsilon = 0.801$)

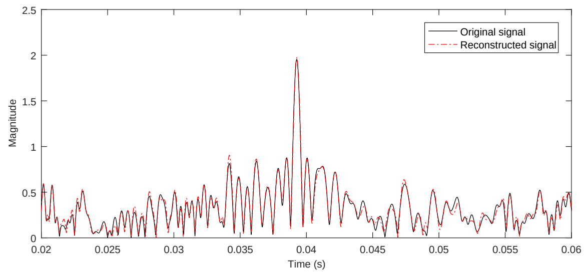

(h) Reconstructed signal ($f_\epsilon = 0.701$)

Figure 6: Results for the l_1 minimization formulation: time-domain plots of the reconstructed signals versus the original signal.

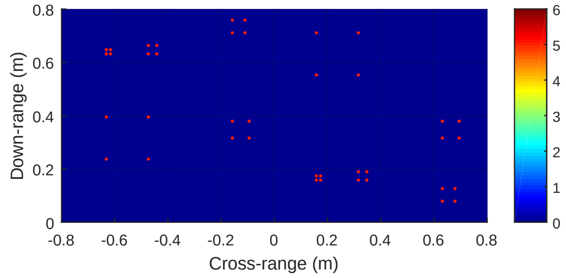

(a) True scatterer plot

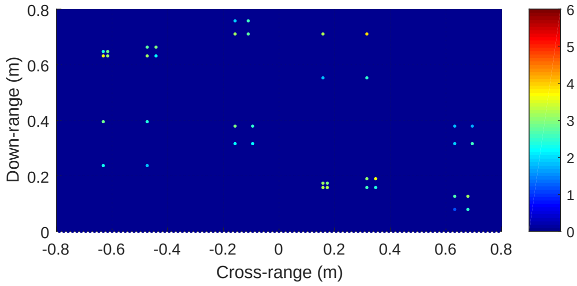

(b) Reconstructed scatterer plot ($f_\epsilon = 1.301$)

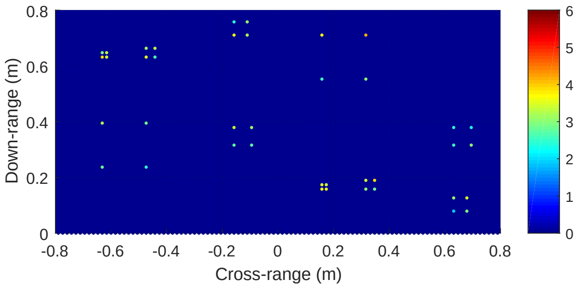

(c) Reconstructed scatterer plot ($f_\epsilon = 1.201$)

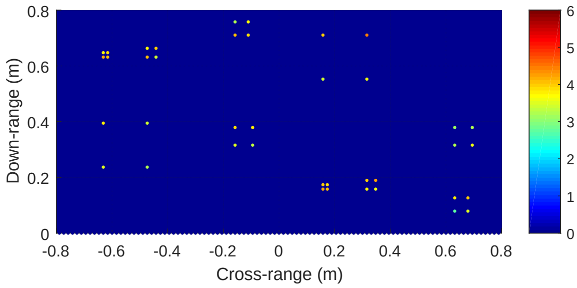

(d) Reconstructed scatterer plot ($f_\epsilon = 1.101$)

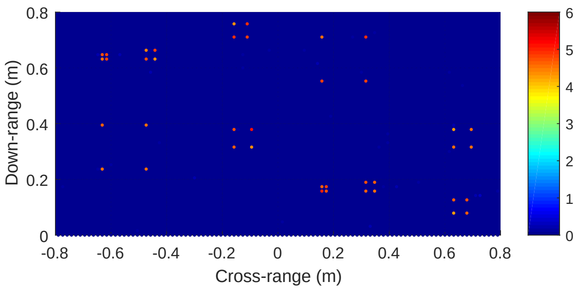

(e) Reconstructed scatterer plot ($f_\epsilon = 1.001$)

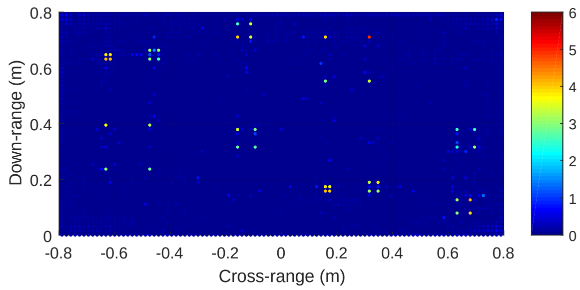

(f) Reconstructed scatterer plot ($f_\epsilon = 0.901$)

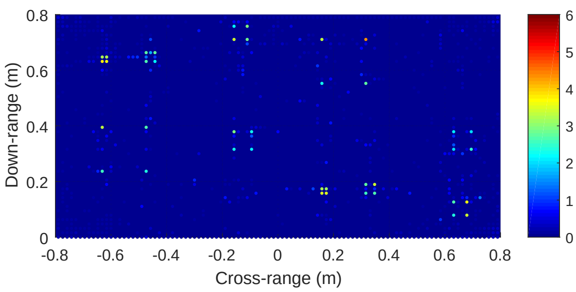

(g) Reconstructed scatterer plot ($f_\epsilon = 0.801$)

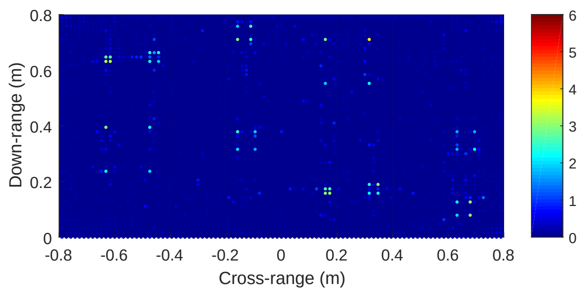

(h) Reconstructed scatterer plot ($f_\epsilon = 0.701$)

Figure 7: Results for the l_1 minimization formulation: scatterer plots of the extracted atoms (color bar indicates the magnitudes of the atom coefficients).

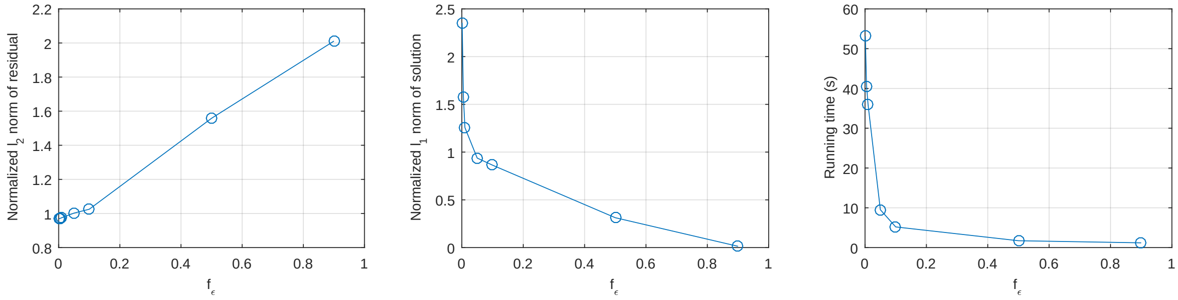

Figure 8: Results for the l_1 regularization formulation: the normalized l_2 norm of the residual, the l_1 norm of the solution and the running time against $f_\epsilon = \epsilon/\sigma$.

Figs. 9 and 10 plot the reconstructed time-domain signal and the corresponding reconstructed scatterer image obtained from the first MC run for each value of κ. It is observed from Fig. 9 that better time-domain signal reconstruction is obtained for smaller values of κ. Specifically, except for the cases of $f_\kappa = 0.9$ and 0.5 which yield unsatisfactory signal reconstruction, we obtain similar reconstructed signals, for $\kappa \leq 0.1$, which closely match with the original signal. However, too small values of λ will reduce the sparsity level in the solution and thus produce unexpected false-alarm scatterers as shown in Figs. 10(g)-(h). The appearance of false-alarm scatters in fact significantly affects the estimated coefficient of the correct scatterers. In particular, the correct scatterers fade away amongst other false-alarm scatterers for $f_\kappa = 0.001$ as shown in Fig. 10(h). In contrast, not all scatterers can be identified if setting κ too small as demonstrated in Fig. 10(b) for the case of $f_\kappa = 0.9$. The values $f_\kappa = 0.01 \sim 0.1$ produce fairly good target reconstruction both in time-domain signal and scatterer imaging representation as shown in Figs. 10(d)-(f). Moreover, we also observe in Fig. 8 that the l_2 norm of the residual closely achieves the desirable value of the noise level while the l_1 norm of the solution is close to the l_1 norm of the ground-truth solution at these values of f_κ.

4.1.4. Results for LASSO

We exploit the use of the LASSO formulation (LS$_\tau$) for our considered problem of radar imaging for rotating target. The LASSO formulation is recalled here for the convenience of readers:

$$(\mathrm{LS}_\tau) \quad \min_{\boldsymbol{x}} \|\boldsymbol{\Phi x} - \mathbf{y}\|_2^2 \quad \text{subject to} \quad \|\boldsymbol{x}\|_1 \leq \tau.$$

The SPG method [27] is used to solve the problem (LS$_\tau$) for different values of τ, i.e., the constraint on the l_1 norm of the solution.

Simulation results are reported in Figs. 11-13 for $\tau \in \{0.625, 0.75, 0.875, 1, 1.125, 1.25, 1.375\}$. As in Sections 4.1.2 and 4.1.3, the trade-off between the l_2 norm of the residual and the l_1 norm of the the solution is also observed for the solution obtained via the LASSO formulation (see Fig. 11). Fig. 11 also indicates that, as expected, a longer running time is required to solve the LASSO formulation with larger value of τ. In addition, we can obtain very good target reconstruction both in time-domain and scatterer imaging representations for $f_\tau \geq 1$; while, for $f_\tau < 1$, correct scatterers are identified but with incorrect coefficients in the reconstructed scatterer image, leading to poorer performance in the time-domain signal

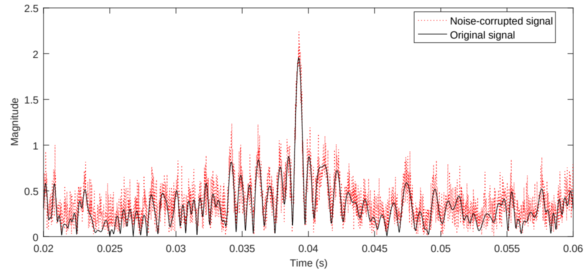

(a) Noise-corrupted signal

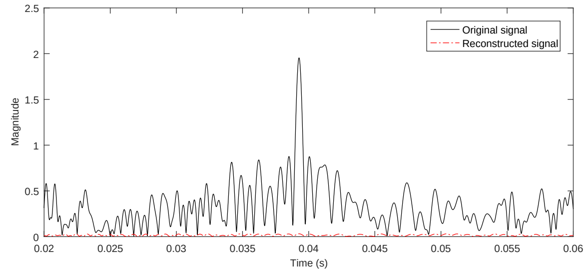

(b) Reconstructed signal ($f_\kappa = 0.9$)

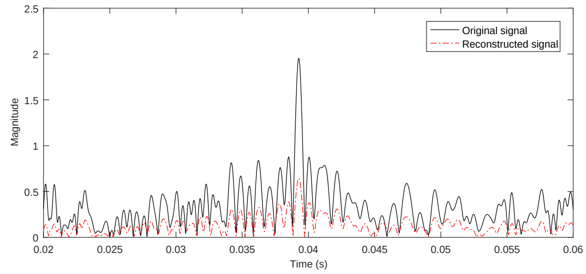

(c) Reconstructed signal ($f_\kappa = 0.5$)

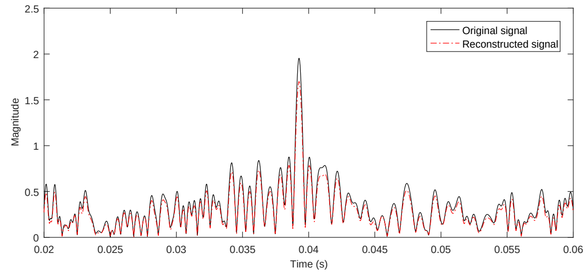

(d) Reconstructed signal ($f_\kappa = 0.1$)

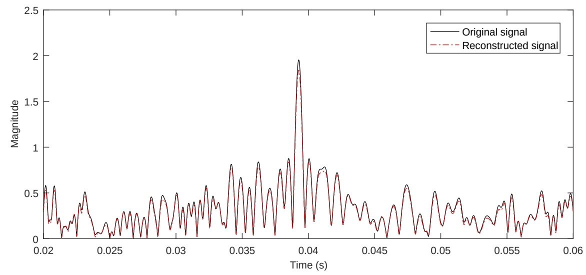

(e) Reconstructed signal ($f_\kappa = 0.05$)

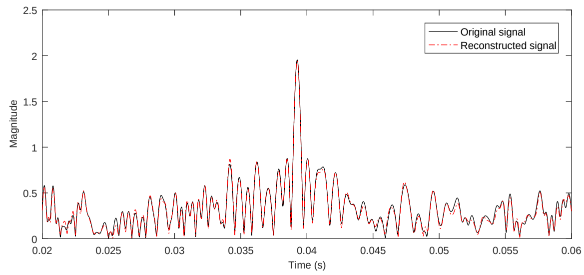

(f) Reconstructed signal ($f_\kappa = 0.01$)

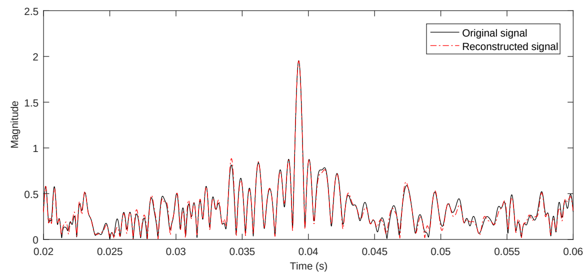

(g) Reconstructed signal ($f_\kappa = 0.005$)

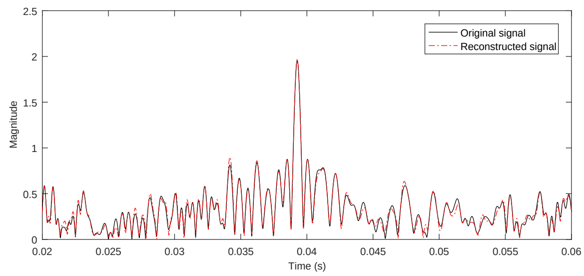

(h) Reconstructed signal ($f_\kappa = 0.001$)

Figure 9: Results for the l_1 regularization formulation: time-domain plots of the reconstructed signals versus the original signal.

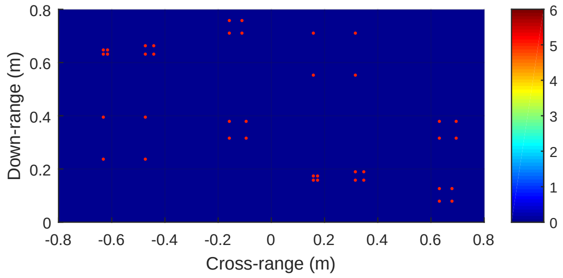

(a) True scatterer plot

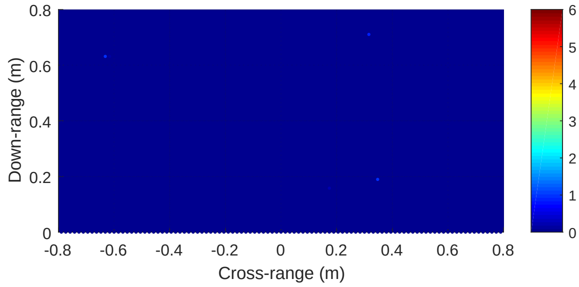

(b) Reconstructed scatterer plot ($f_\kappa = 0.9$)

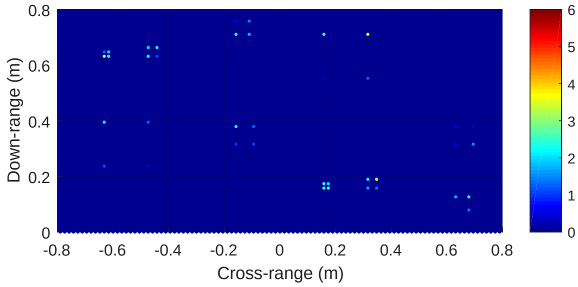

(c) Reconstructed scatterer plot ($f_\kappa = 0.5$)

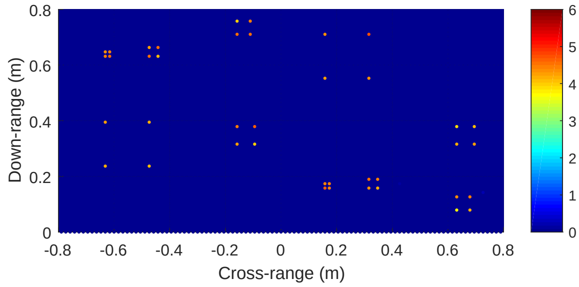

(d) Reconstructed scatterer plot ($f_\kappa = 0.1$)

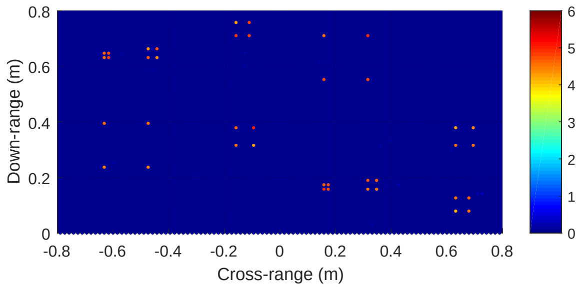

(e) Reconstructed scatterer plot ($f_\kappa = 0.05$)

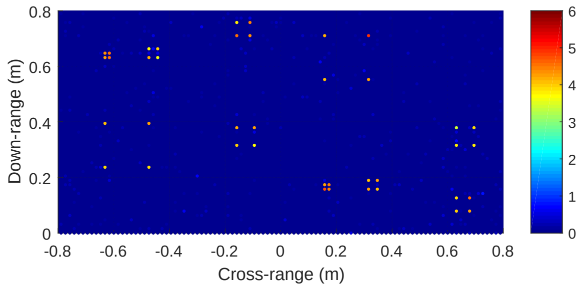

(f) Reconstructed scatterer plot ($f_\kappa = 0.01$)

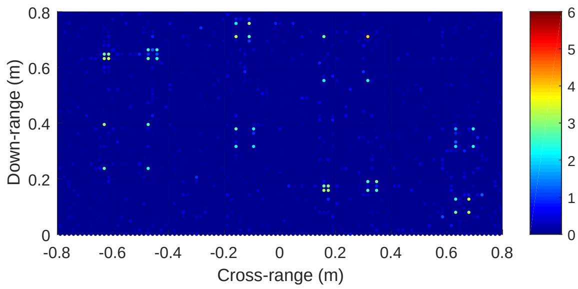

(g) Reconstructed scatterer plot ($f_\kappa = 0.005$)

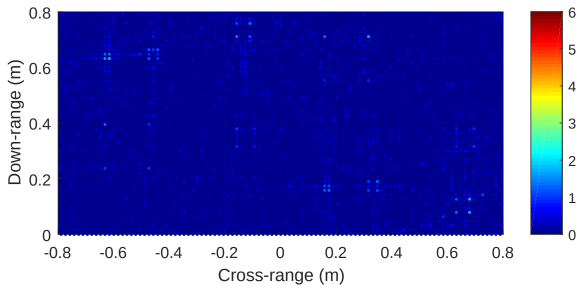

(h) Reconstructed scatterer plot ($f_\kappa = 0.001$)

Figure 10: Results for the l_1 regularization formulation: scatterer plots of the extracted atoms (color bar indicates the magnitudes of the atom coefficients).

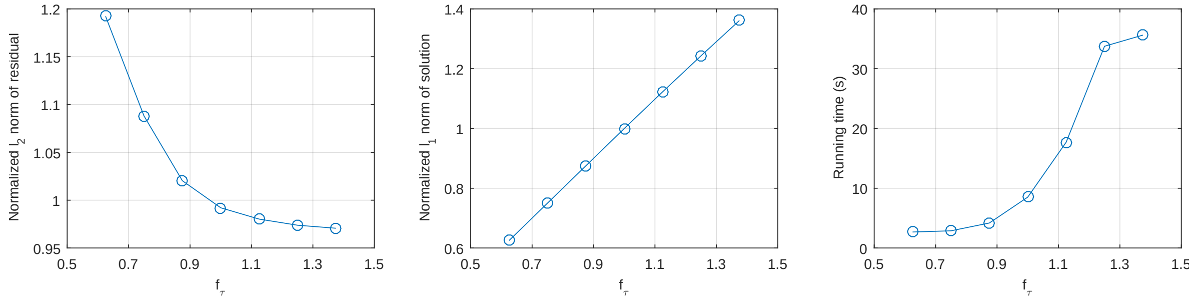

Figure 11: Results for the LASSO formulation: the normalized l_2 norm of the residual, the l_1 norm of the solution and the running time against $f_\epsilon = \epsilon/\sigma$.

reconstruction. Moreover, for large values of τ (e.g., $f_\tau = 1.375$, false-alarm scatterers start to arise). We also observed during our simulation tests that SPG method may fail to converge for too large a value of τ. As observed from Figs. 11-13, it is most appropriate to set τ close to the l_1 norm of the ground-truth solution. In practice, the l_1 norm of the ground-truth solution is generally unknown. However, it is noticed from Fig. 11 that the l_2 norm of the residual tends to converge for $f_\tau > 1$ (i.e., the constraint parameter τ is larger than the l_1 norm of the ground-truth solution). Thus we can roughly identify the l_1 norm of the ground-truth solution based on the curvature of the l_2 norm of the residual (i.e. around the point at which the residual's l_2 norm starts to converge).

4.1.5. Debiasing/Reweighting

This section aims to demonstrate the effectiveness of the debiasing/reweighting procedure to the considered radar imaging problem. In particular, our objective is to use a limited number of scatterer atoms with significant coefficients to represent the target. The number of atoms to be retained can be determined by examining the curvature of the magnitude of the descending sorted solution vector. For illustration, Fig. 14 plots the magnitude of the solution of the l_1 minimization formulation obtained using the SPG algorithm with $\epsilon = 0.801\sigma$ after sorting in descending order. A notable drop in the magnitude can be observed at the index of 40, indicating the number of significant atoms in the solution. Fig. 15 shows the reconstructed scatterer plot after performing debiasing/reweighting over the 40 identified most significant atoms in comparison with the original reconstructed scatterer plot without debiasing/reweighting. The false-alarm scatterers no longer exists as the coefficients of the insignificant atoms are set to zero. In addition, much better estimates (almost identical to the ground truth) are obtained for the coefficients of the remaining atoms thanks to the (least-squares) reweighting process.

4.2. Simulations with the Total Variation Norm

4.2.1. Simulation Setup

We consider a scenario with a piecewise constant target consisting of one L-shape solid object and two square solid objects rotating around the origin of the target local coordinate at

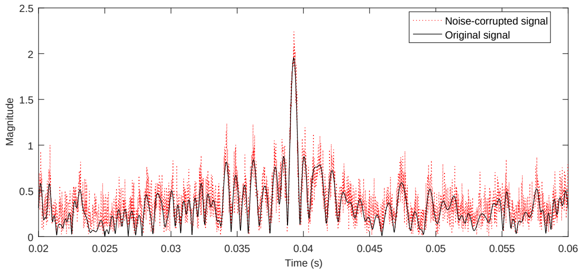

(a) Noise-corrupted signal

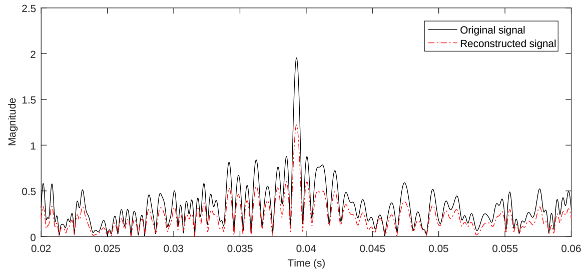

(b) Reconstructed signal ($f_\tau = 0.625$)

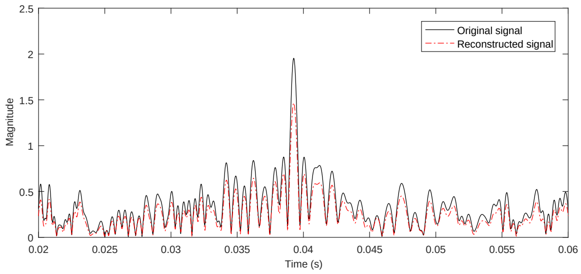

(c) Reconstructed signal ($f_\tau = 0.75$)

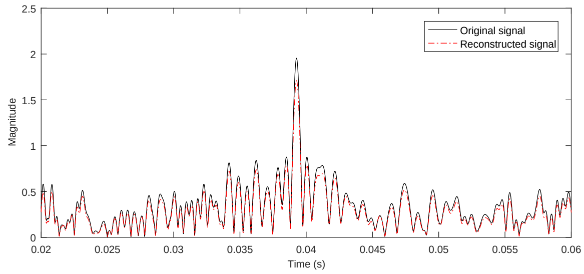

(d) Reconstructed signal ($f_\tau = 0.875$)

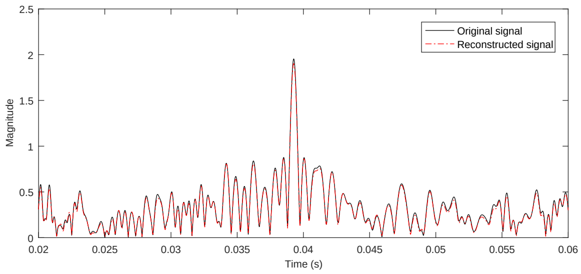

(e) Reconstructed signal ($f_\tau = 1$)

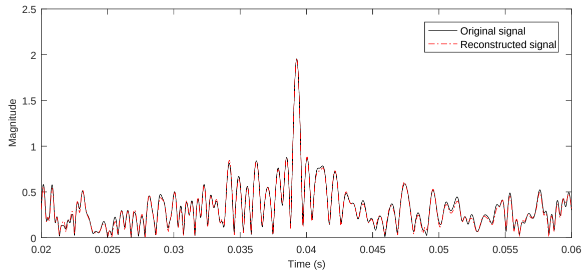

(f) Reconstructed signal ($f_\tau = 1.125$)

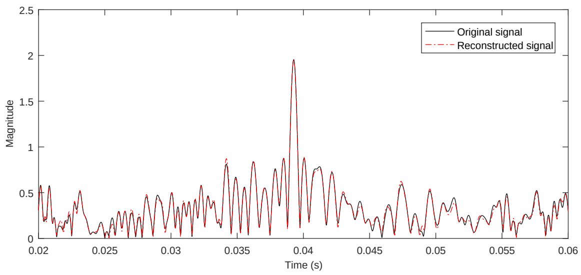

(g) Reconstructed signal ($f_\tau = 1.25$)

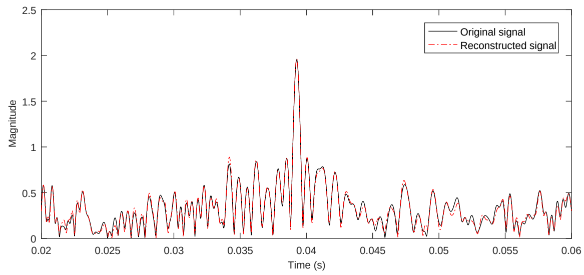

(h) Reconstructed signal ($f_\tau = 1.325$)

Figure 12: Results for the LASSO formulation: time-domain plots of the reconstructed signals versus the original signal.

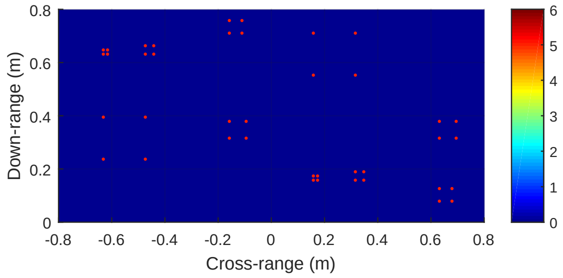

(a) True scatterer plot

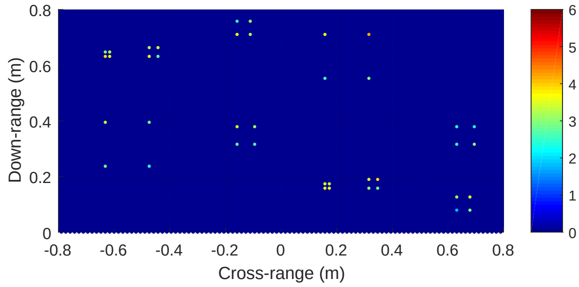

(b) Reconstructed scatterer plot ($f_\tau = 0.625$)

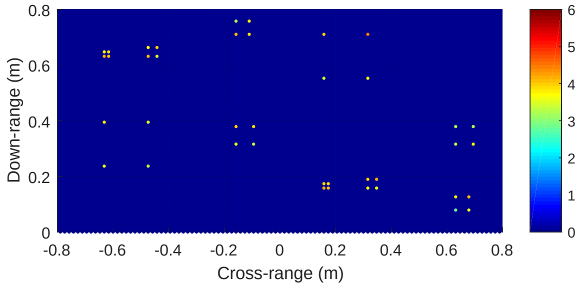

(c) Reconstructed scatterer plot ($f_\tau = 0.75$)

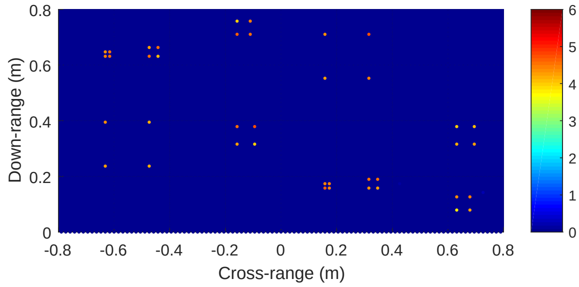

(d) Reconstructed scatterer plot ($f_\tau = 0.875$)

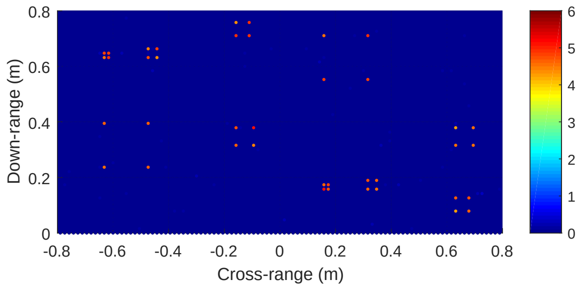

(e) Reconstructed scatterer plot ($f_\tau = 1$)

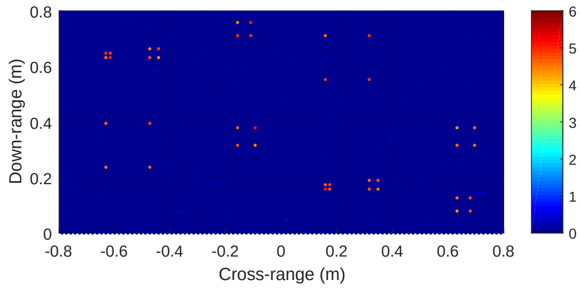

(f) Reconstructed scatterer plot ($f_\tau = 1.125$)

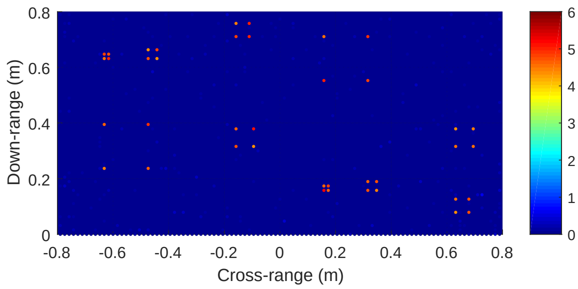

(g) Reconstructed scatterer plot ($f_\tau = 1.25$)

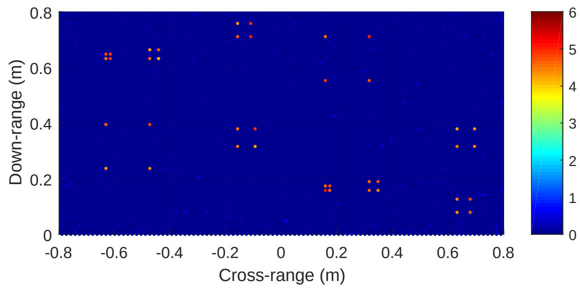

(h) Reconstructed scatterer plot ($f_\tau = 1.325$)

Figure 13: Results for the LASSO formulation: scatterer plots of the extracted atoms (color bar indicates the magnitudes of the atom coefficients).

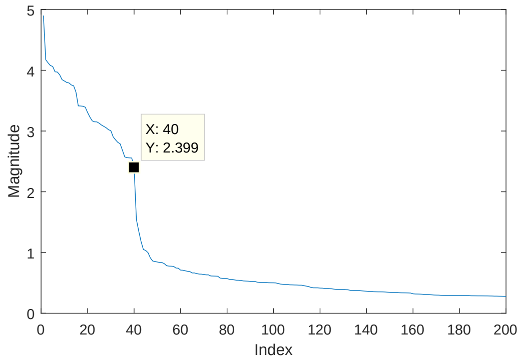

Figure 14: The magnitude of the descending sorted solution obtained using the SGP algorithm with $\epsilon = 0.801\sigma$ (only the first 200 atoms are plotted).

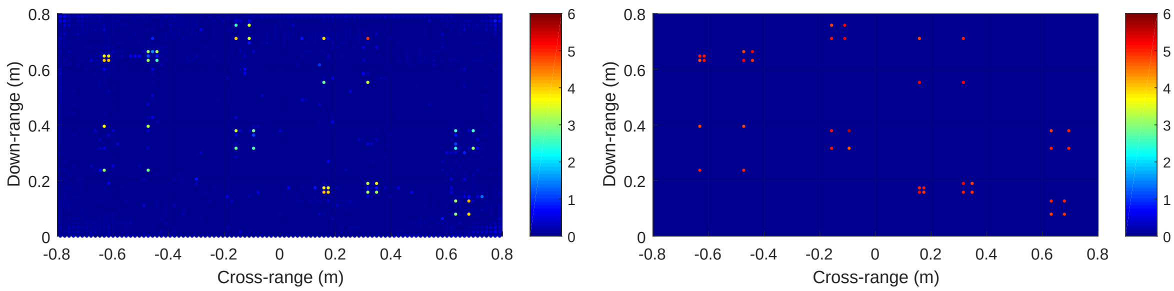

(a) Before debiasing/reweighting

(b) After debiasing/reweighting

Figure 15: Reconstructed scatterer plots before and after applying debiasing/reweighting for the solution obtained by the SGP algorithm with $\epsilon = 0.801\sigma$.

40 rad/sec as depicted in Fig. 16. The same radar parameters as in Section 4.1 are used to simulate the backscattered signal in one rotation cycle of the target. The SNR is set to 2 dB in this scenario. Fig. 17 plots the simulated original signal and the simulated noise-corrupted signal in the time domain.

4.2.2. Results

Figs. 18 and 19 plot the time-domain reconstructed signal and the reconstructed scatterer images of the solutions, respectively, obtained by the SpaRSA algorithm [30] for the sole l_1 regularization in (10), the sole TV regularization in (12) and the mixed l_1 and TV regularization in (13). For a fair comparison, the regularization parameters in (10), (12) and (13) are chosen such that the objective functions in (10), (12) and (13) are equal at the true solution, and the same stopping criterion (i.e., stop when the objective function becomes equal or less than the same threshold) is used to obtain the solutions. We can see from Fig. 18 that the reconstructed signals in the time domain obtained via the l_1 only regularization, the TV only regularization and the mixed l_1 and TV regularization are similar and closely matched with the original ground-truth signal. In contrast, those three regularizations perform differently in the special scatterer representation domain. Since our ultimate objective is to build a

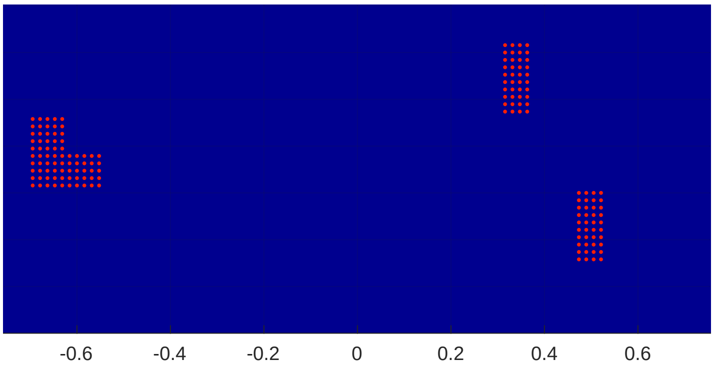

Figure 16: Simulated target with one L-shape solid object and two square solid objects.

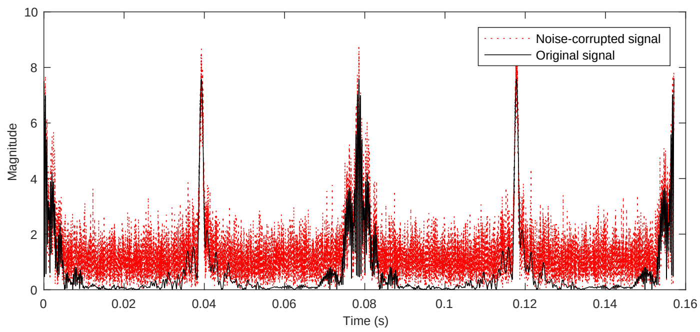

Figure 17: Simulated backscattered signal from the target depicted in Fig. 16 versus time.

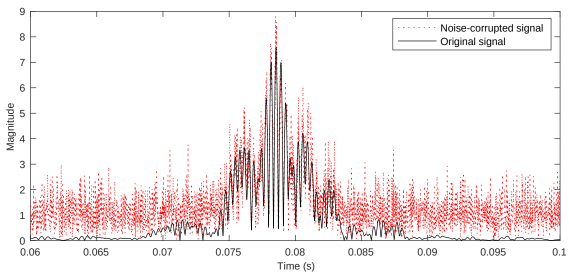

(a) Noise-corrupted signal

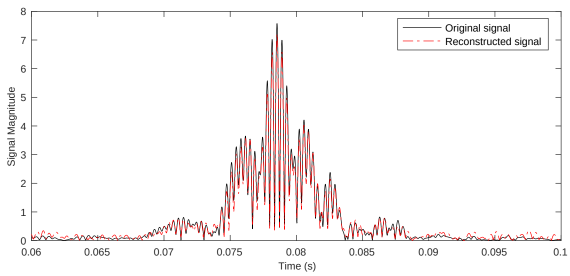

(b) Reconstructed signal via l_1 regularization

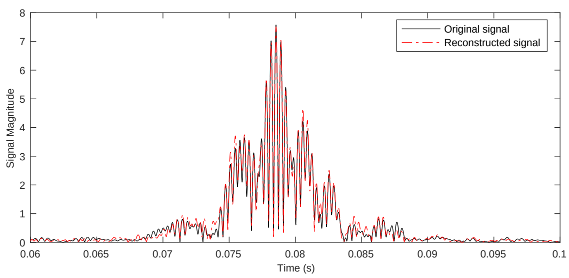

(c) Reconstructed signal via TV regularization

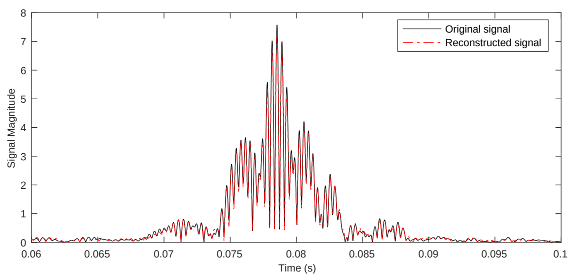

(d) Reconstructed signal via mixed l_1 and TV regularization

Figure 18: Time-domain plots of the reconstructed signals versus the original signal.

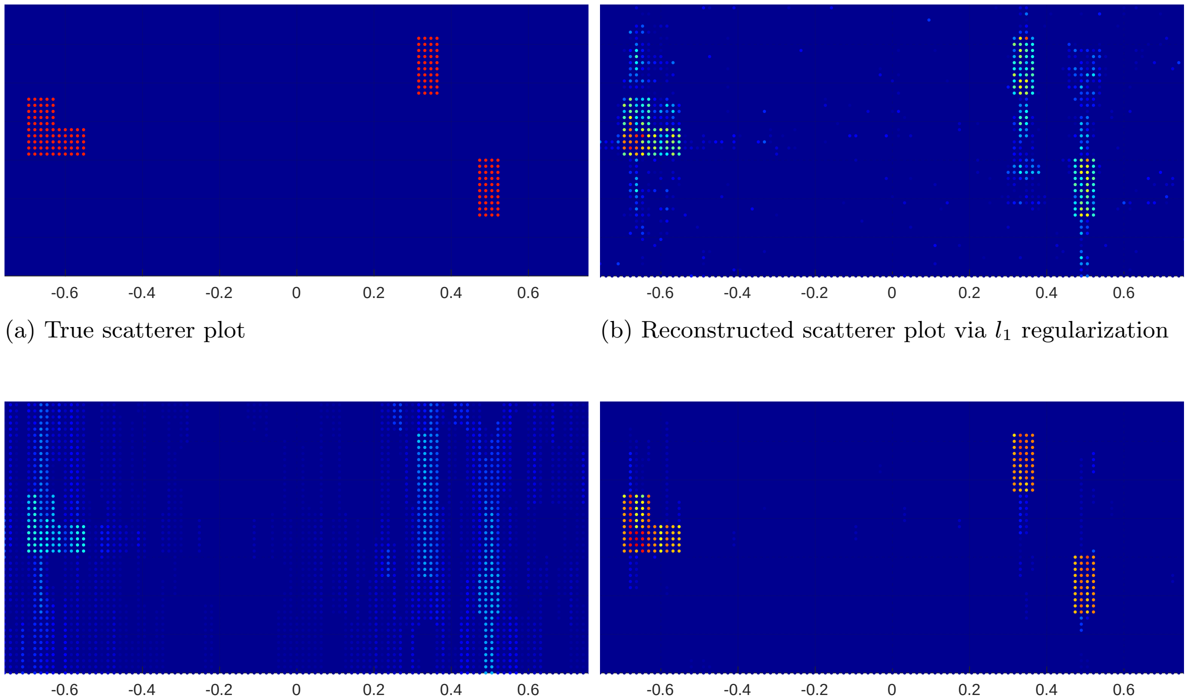

(a) True scatterer plot

(b) Reconstructed scatterer plot via l_1 regularization

(c) Reconstructed scatterer plot via TV regularization

(d) Reconstructed scatterer plot via mixed l_1 and TV regularization

Figure 19: Scatterer plots of the extracted atoms (color bar indicates the magnitudes of the atom coefficients).

scatterer image of the target, we will focus our discussion on the performance comparison in the scatterer representation domain.

It is observed in Fig. 19 that the l_1 regularization correctly capture the three ground-truth target objects, however, with the presence of false-alarm objects nearby as well as many other false-alarm scatterers located randomly all around the place. Although the individual isolated scatterers can be readily recognized as false-alarms, it is more difficult to determine whether the nearby false-alarm objects (formed by groups of scatterers clustering together) belong to the target or not. On the other hand, the target objects are badly smeared out in the scatterer image produced by the TV regularization. This observation can be explained by noting that the simulated target is not really a piecewise-constant target. In fact, it is actually more sparse oriented than piecewise-constant oriented. Note that this type of target, which has both sparse and piecewise characteristics, commonly occurs in practice (e.g., helicopter blades). It is shown in Fig. 19 that, the mixed l_1 and TV regularization produced the best scatterer representation image of the target by taking the advantages of both the l_1 regularization and the TV regularization. Specifically, the l_1 regularization term promotes the sparsity in the solution and thus reducing the smearing effect due to the TV regularization. On the other hand, the TV regularization term promotes the preservation of the edge details and the removal of unwanted noisy details. As a result, the incorrect false-alarm objects nearby the true objects as well as other individual isolated false-alarms scatterers in the background are significantly depressed and almost completely removed. However, it is still an open question as to what values of the regularization parameters κ and ν should be selected to produce an optimal scatterer representation image of the target. This will be considered further in our future research work.

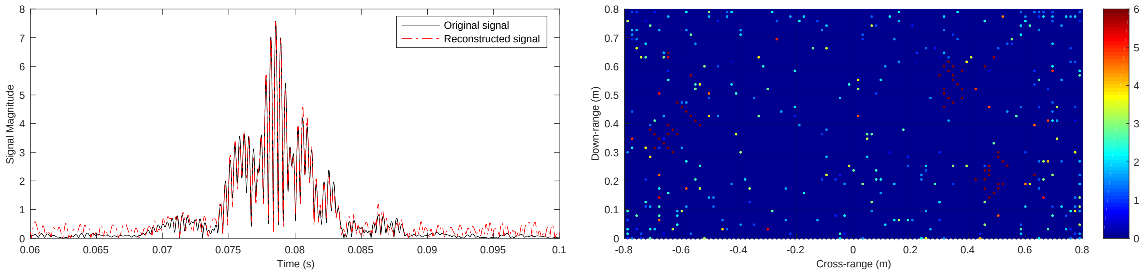

(a) Reconstructed time-domain signal

(b) Reconstructed scatterer plot

Figure 20: Simulation results obtained by OMP for piecewise-constant target.

In addition, we also observe that the orthogonal matching pursuit (OMP) algorithm [52], viz., the most popular greedy pursuit method in the literature, does not handle the piecewise-constant target very well. In particular, it is shown in Fig. 20 that the OMP algorithm results in an equitably good reconstructed signal in the time domain. However, the OMP algorithm fails to produce a meaningful scatterer image about the target. On the other hand, we observed in our simulation (although not shown here) that the OMP algorithm works effectively both in terms of time-domain signal reconstruction and scatterer imaging representation for the case of point-scatterer targets appearing in Section 4.1.

4.3. Preliminary Results for Off-Grid Targets

We present preliminary results for the scenario where at least some of the true scatterers do not lie on the dictionary grid. We now consider a target model similar to Fig.3 of Section 4.1, except that four groups of points on the right-hand side are shifted by an offset both in the x- and y-axes, to make them ‘off-grid’.

Figs. 21 shows the simulation results when the offset is $1/10$ of the step size of the dictionary grid. We observe that the reconstructed image starts to degrade, especially in the right-hand side half region where off-grid scatterers exist. When the offset value is fairly small, as in this example, we still obtain a reasonable image. However, for larger offset values, such as at half of the grid size as shown in Fig. 22, the right-hand side part of the reconstructed scatterer image is severely degraded; spurious scatterers start to appear, even though the signal reconstruction is still highly satisfactory in the time domain.

The situation becomes even worse for the case of a piecewise-constant target. Fig. 23 shows the simulation results for the same target model used in Section 4.2, but the target is shifted by $1/10$ grid size both in the x- and y-axes. Such a small offset can still degrade the scatterer image reconstruction significantly. It is observed from Fig. 23 that numerous other spurious scatterers appear in the reconstructed scatterer image as well, while some parts of the target are missing.

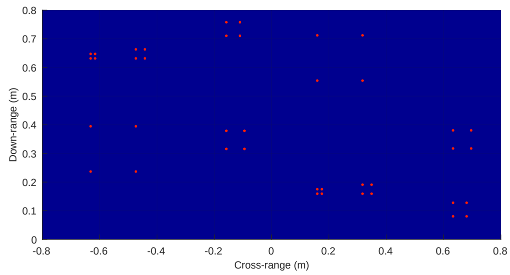

(a) True scatterer plot

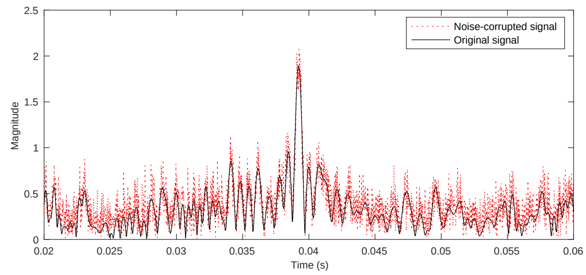

(b) Noise-corrupted signal

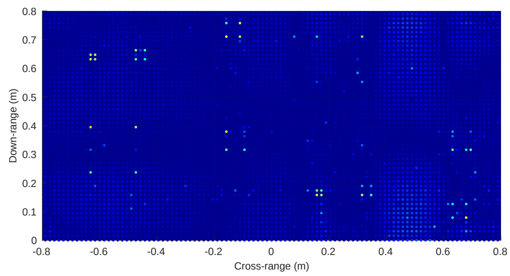

(c) Reconstructed scatterer plot via l_1 minimization ($f_\epsilon = 1.001$)

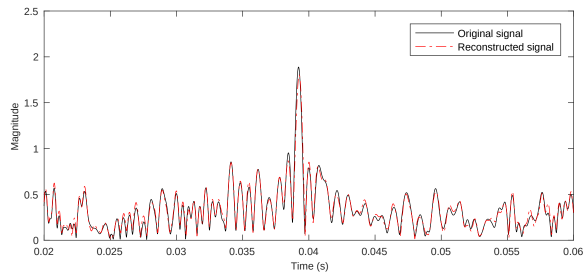

(d) Reconstructed time-domain signal via l_1 minimization ($f_\epsilon = 1.001$)

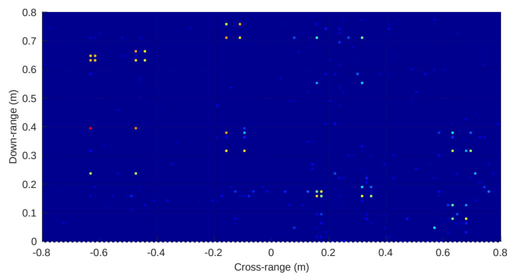

(e) Reconstructed scatterer plot via l_1 regularization ($f_\kappa = 0.05$)

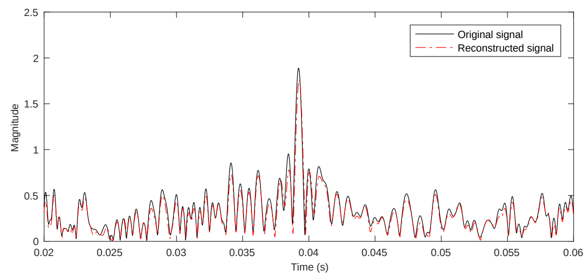

(f) Reconstructed time-domain signal via l_1 regularization ($f_\kappa = 0.05$)

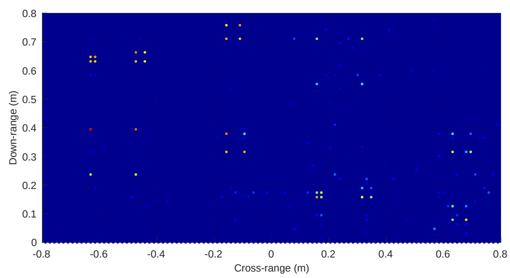

(g) Reconstructed scatterer plot via LASSO ($f_\tau = 1$)

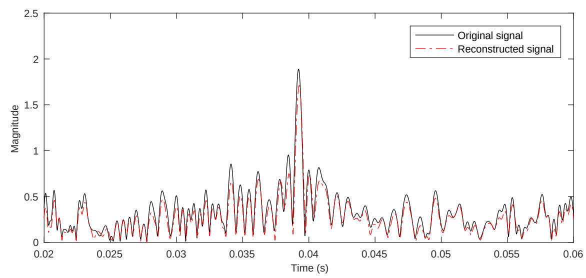

(h) Reconstructed time-domain signal via LASSO ($f_\tau = 1$)

Figure 21: Simulation results for the off-grid scenario 1 (offset = 1/10 grid size).

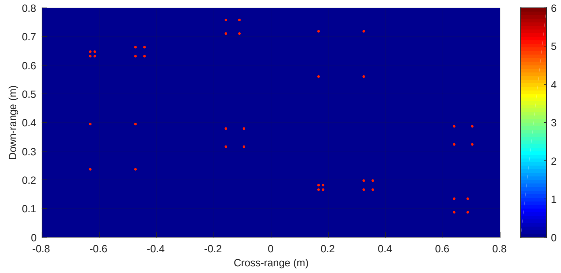

(a) True scatterer plot

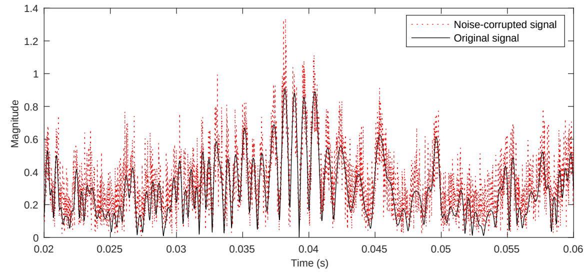

(b) Noise-corrupted signal

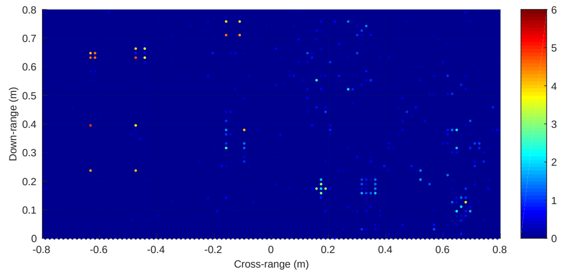

(c) Reconstructed scatterer plot via l_1 minimization ($f_\epsilon = 1.001$)

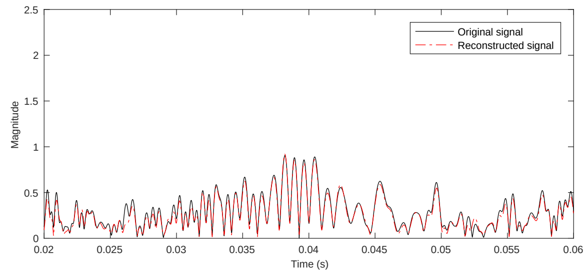

(d) Reconstructed time-domain signal via l_1 minimization ($f_\epsilon = 1.001$)

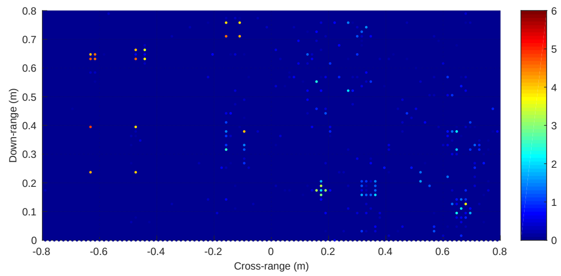

(e) Reconstructed scatterer plot via l_1 regularization ($f_\kappa = 0.05$)

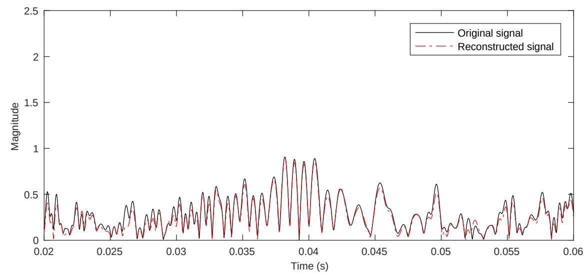

(f) Reconstructed time-domain signal via l_1 regularization ($f_\kappa = 0.05$)

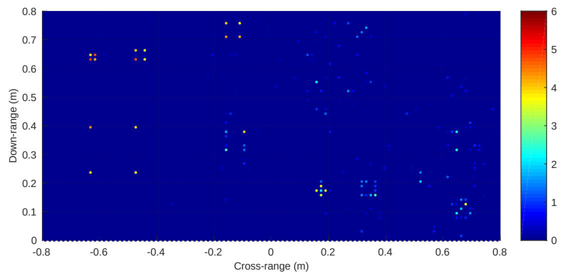

(g) Reconstructed scatterer plot via LASSO ($f_\tau = 1$)

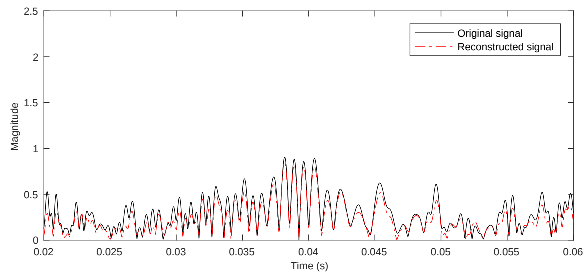

(h) Reconstructed time-domain signal via LASSO ($f_\tau = 1$)

Figure 22: Simulation results for the off-grid scenario 2 (offset=1/2 grid size).

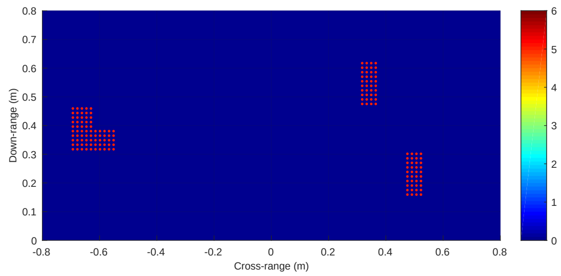

(a) True scatterer plot

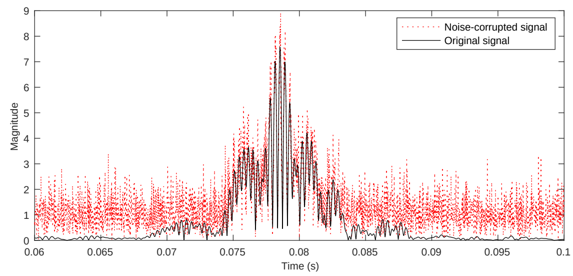

(b) Noise-corrupted signal

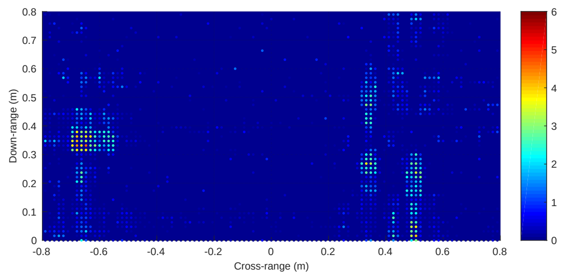

(c) Reconstructed scatterer plot via l_1 regularization

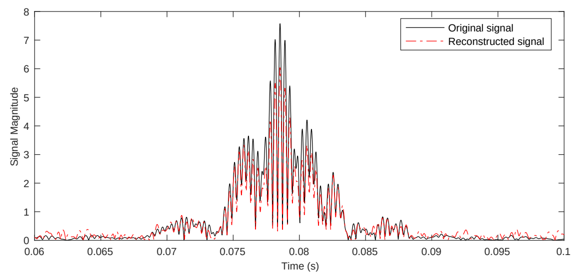

(d) Reconstructed time-domain signal via l_1 regularization

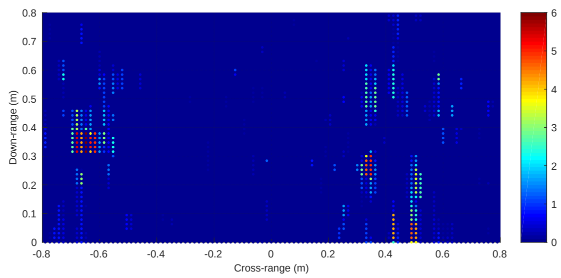

(e) Reconstructed scatterer plot via mixed l_1-TV regularization

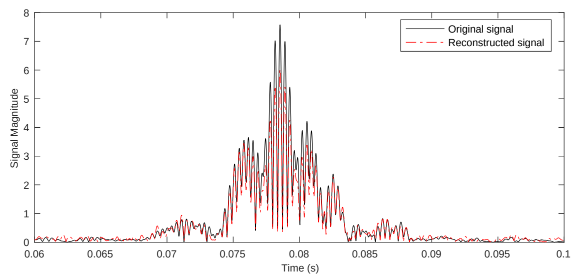

(f) Reconstructed time-domain signal via mixed l_1-TV regularization

Figure 23: Simulation results for the off-grid scenario 3 (piecewise-constant target).

A possible measure to alleviate the problem associated with off-grid targets is to reduce the grid step size of the dictionary parameters. However, we observed in our simulation that reducing the grid step size leads to a higher correlation with the atoms in the dictionary and may create multiple solutions even for the case of on-grid targets, where we obtain a perfect reconstruction in the time-domain signal but a wrong scatterer image of the target in the spatial domain.

5. Conclusion

Three convex relaxation formulations based on l_1 norm were considered including l_1 minimization, l_1 regularization, and LASSO. The simulation results found that these l_1 norm optimization approaches can lead to satisfactory image reconstruction in the time-domain signal as well as in the scatterer image reconstruction in the spatial domain when appropriate values of tuning parameters ϵ, κ and τ are used.

We also observed that the l_1 norm optimization approaches becomes less effective for piecewise-constant (or 'block') targets. In such a scenario, the mixed l_1 and total variation norm optimization approach exhibits a better performance in constructing the scatterer image of the target. In such cases, the l_1 regularization term promotes the sparsity in the solution, thus reducing blurring effects due to the total variation regularization, while the total variation regularization term promotes the preservation of the edge details and the removal of unwanted noisy components.

Preliminary results for the case of off-grid targets are also provided. In particular, the imaging performance may degrade significantly as the offset distances from the true locations of the scatterers constituting the target to the dictionary grid increase. Reducing the step size of the dictionary grid is a possible measure to alleviate the problems associated with off-grid targets. However, decreasing the grid step size may increase the correlation level between atoms in the dictionary which in turn degrades the performance of convex relaxation algorithms. Further work is warranted to tackle the off-grid problems, which are almost always the case in real applications of radar imaging.

Acknowledgements

This work was undertaken under Research Agreement (MyID 6712) between Defence Science and Technology (DST) Group and University of South Australia. The authors would like to thank Dr Richard Egudo for his critical review comments, and Dr. Leigh Powis and Dr. Andrew Shaw (Research Leader Surveillance and Reconnaissance Systems, NSID) for their review, leadership and guidance.

6. References

1. Nguyen, N. H. et al. (Sept. 2016) *A review of sparsity-based methods for analysing radar returns from helicopter rotor returns.* Tech. rep. DST Group. DST-Group-TR-3292.

2. Chen, V. C. et al. (Jan. 2006) ‘Micro-Doppler effect in radar: phenomenon, model, and simulation study’. In: *IEEE Trans. Aerosp. Electron. Syst.* **42** (1), 2–21.
3. Chen, V. C. et al. (2003) ‘Analysis of micro-Doppler signatures’. In: *IEE Proc. Radar Sonar Navig* **150** (4), 271–276.
4. Giusti, E. et al. (2014) ‘Super resolution ISAR imaging via Compressing Sensing’. In: *EUSAR 2014; 10th European Conference on Synthetic Aperture Radar*, 1–4.
5. Tropp, J. A. and Wright, S. J. (June 2010) ‘Computational methods for sparse solution of linear inverse problems’. In: *Proc. IEEE* **98** (6), 948–958.
6. Melino, R., Kodituwakku, S. and Tran, H. T. (Oct. 2015) ‘Orthogonal matching pursuit and matched filter techniques for the imaging of rotating blades’. In: *Proc. IEEE Radar Conf.* 1–6.
7. Natarajan, B. K. (1995) ‘Sparse approximate solutions to linear systems’. In: *SIAM Journal on Computing* **24** (2), 227–234.
8. Donoho, D. L. (Apr. 2006) ‘Compressed sensing’. In: *IEEE Trans. Inf. Theory* **52** (4), 1289–1306.
9. Candes, E. J. and Tao, T. (Dec. 2005) ‘Decoding by linear programming’. In: *IEEE Trans. Inf. Theory* **51** (12), 4203–4215.
10. Candes, E. J. (2008) ‘The restricted isometry property and its implications for compressed sensing’. In: *Comptes Rendus Mathematique* **346** (910), 589–592.
11. Candes, E. J., Romberg, J. and Tao, T. (Feb. 2006) ‘Robust uncertainty principles: exact signal reconstruction from highly incomplete frequency information’. In: *IEEE Trans. Inf. Theory* **52** (2), 489–509.
12. Tropp, J. A. (Mar. 2006) ‘Just relax: convex programming methods for identifying sparse signals in noise’. In: *IEEE Trans. Inf. Theory* **52** (3), 1030–1051.
13. Y. C. Eldar, G. K., ed. (2012) *Compressed Sensing: Theory and Applications*. Cambridge University Press. New York.
14. Potter, L. C. et al. (June 2010) ‘Sparsity and compressed sensing in radar imaging’. In: *Proc. IEEE* **98** (6), 1006–1020.
15. Tropp, J. A. (Oct. 2004) ‘Greed is good: algorithmic results for sparse approximation’. In: *IEEE Trans. Inf. Theory* **50** (10), 2231–2242.
16. Donoho, D. L. and Huo, X. (Nov. 2001) ‘Uncertainty principles and ideal atomic decomposition’. In: *IEEE Trans. Inf. Theory* **47** (7), 2845–2862.
17. Donoho, D. L. and Elad, M. (2003) ‘Optimally sparse representation in general (nonorthogonal) dictionaries via l_1 minimization’. In: *Proc. Nat. Acad. Sci.* **100** (5), 2197–2202.
18. Donoho, D. L., Elad, M. and Temlyakov, V. N. (Jan. 2006) ‘Stable recovery of sparse overcomplete representations in the presence of noise’. In: *IEEE Trans. Inf. Theory* **52** (1), 6–18.
19. Fuchs, J. J. (June 2004) ‘On sparse representations in arbitrary redundant bases’. In: *IEEE Trans. Inf. Theory* **50** (6), 1341–1344.

20. Tropp, J. A. (2008) ‘On the conditioning of random subdictionaries’. In: *Appl. Comput. Harmonic Anal.* **25** (1), 1–24.

21. Candes, E. J. and Plan, Y. (2009) ‘Near-ideal model selection by l_1 minimization’. In: *Ann. Stat.* **37** (5A), 2145–2177.

22. Candes, E. J., Romberg, J. K. and Tao, T. (2006) ‘Stable signal recovery from incomplete and inaccurate measurements’. In: *Commun. Pure Appl. Math.* **59** (8), 1207–1223.

23. Candes, E. J. and Tao, T. (Dec. 2006) ‘Near-optimal signal recovery from random projections: universal encoding strategies?’ In: *IEEE Trans. Inf. Theory* **52** (12), 5406–5425.

24. Chen, S. S., Donoho, D. L. and Saunders, M. A. (2001) ‘Atomic decomposition by basis pursuit’. In: *SIAM Review* **43** (1), 129–159.

25. Tibshirani, R. (1996) ‘Regression shrinkage and selection via the LASSO’. In: *J. R. Statist. Soc. B,* 267–288.

26. Rockafellar, R. T. (1970) *Convex Analysis.* Princeton University Press. New Jersey.

27. van den Berg, E. and Friedlander, M. P. (2009) ‘Probing the Pareto frontier for basis pursuit solutions’. In: *SIAM J. Sci. Comput.* **31** (2), 890–912.

28. Becker, S., Bobin, J. and Candes, E. J. (2011) ‘NESTA: A fast and accurate first-order method for sparse recovery’. In: *SIAM J. Imaging Sci.* **4** (1), 1–39.

29. Bioucas-Dias, J. M. and Figueiredo, M. A. T. (Dec. 2007) ‘A new TwIST: Two-step iterative shrinkage/thresholding algorithms for image restoration’. In: *IEEE Trans. Image Process.* **16** (12), 2992–3004.

30. Wright, S. J., Nowak, R. D. and Figueiredo, M. A. T. (July 2009) ‘Sparse reconstruction by separable approximation’. In: *IEEE Trans. Signal Process.* **57** (7), 2479–2493.

31. Cetin, M. and Karl, W. C. (Apr. 2001) ‘Feature-enhanced synthetic aperture radar image formation based on nonquadratic regularization’. In: *IEEE Trans. Image Process.* **10** (4), 623–631.

32. Chen, S. S. (1995) ‘Basis pursuit’. PhD thesis. Department of Statistics, Stanford Univ.

33. Saunders, M. A. *PDCO: Primal-dual interior method for convex objectives.* Systems Optimization Laboratory, Stanford Univ. URL: http://web.stanford.edu/group/SOL/software/pdco/.

34. Kim, S. J. et al. (Dec. 2007) ‘An interior-point method for large-scale l_1-regularized least squares’. In: *IEEE J. Sel. Topics Signal Process.* **1** (4), 606–617.

35. Candes, E. and Romberg, J. (Oct. 2005) *l_1-MAGIC : Recovery of sparse signals via convex programming.* Tech. rep. California Inst. Technol. Pasadena, CA.

36. Boyd, S. and Vandenberghe, L. (2004) *Convex Optimization.* Cambridge University Press. Cambridge, UK.

37. Combettes, P. L. and Wajs, V. R. (2005) ‘Signal recovery by proximal forward-backward splitting’. In: *SIAM J. Multiscale Model. Simul.* **4** (4), 1168–1200.

38. Hale, E. T., Yin, W. and Zhang, Y. (2008) ‘Fixed-point continuation for l_1-minimization: Methodology and convergence’. In: *SIAM J.Optim.* **19** (3), 1107–1130.

39. Daubechies, I., Defrise, M. and De Mol, C. (Nov. 2004) 'An iterative thresholding algorithm for linear inverse problems with a sparsity constraint'. In: *Commun. Pure Appl. Math.* **57** (11), 1413–1457.

40. Elad, M. (Dec. 2006) 'Why simple shrinkage is still relevant for redundant representations?' In: *IEEE Trans. Inf. Theory* **52** (12), 5559–5569.

41. Beck, A. and Teboulle, M. (2009) 'A fast iterative shrinkage-thresholding algorithm for linear inverse problems'. In: *SIAM J. Imaging Sci.* **2** (1), 183–202.

42. Nesterov, Y. (1983) 'A method for solving the convex programming problem with convergence rate $\mathcal{O}(1/k^2)$.' In: *Dokl. Akad. Nauk SSSR* **27** (2), 372–376.

43. Wen, Z. et al. (2010) 'A fast algorithm for sparse reconstruction based on shrinkage, subspace optimization, and continuation'. In: *SIAM J. Sci. Comput.* **32** (4), 1832–1857.

44. Figueiredo, M. A. T., Nowak, R. D. and Wright, S. J. (Dec. 2007) 'Gradient projection for sparse reconstruction: application to compressed sensing and other inverse problems'. In: *IEEE J. Sel. Topics Signal Process.* **1** (4), 586–597.

45. Birgin, E. G., Martinez, J. M. and Raydan, M. (2000) 'Nonmonotone spectral projected gradient methods on convex sets'. In: *SIAM J. Optim.* **10** (4), 1196–1211.

46. Efron, B. et al. (Apr. 2004) 'Least angle regression'. In: *Ann. Statist.* **32** (2), 407–499.

47. Osborne, M. R., Presnell, B. and Turlach, B. A. (2000) 'A new approach to variable selection in least squares problems'. In: *IMA J. Numer. Anal.* **20** (3), 389–403.

48. Yoon, Y.-S. and Amin, M. G. (2008) 'Compressed sensing technique for high-resolution radar imaging'. In: *SPIE Defense and Security Symposium*. Vol. 6968, 1–10.

49. Huang, Q. et al. (Mar. 2010) 'UWB through-wall imaging based on compressive sensing'. In: *IEEE Trans. Geosci. Remote Sens.* **48** (3), 1408–1415.

50. Stojanovic, I., Karl, W. C. and Cetin, M. (2009) 'Compressed sensing of mono-static and multi-static SAR'. In: *SPIE Defense, Security, and Sensing*. Vol. 7337, 1–12.

51. Marengo, E. A. (Dec. 2007) 'Inverse scattering by compressive sensing and signal subspace methods'. In: *IEEE Int. Workshop Comp. Adv. Multi-Sensor Adaptive Process.* 109–112.

52. Pati, Y. C., Rezaiifar, R. and Krishnaprasad, P. S. (Nov. 1993) 'Orthogonal matching pursuit: recursive function approximation with applications to wavelet decomposition'. In: *Proc. 27th Asilomar Conf. Signals, Syst., Comput.* Vol. 1, 40–44.

DISTRIBUTION LIST

Convex Relaxation Methods: A Review and Application to Sparse Radar Imaging of Rotating Targets

Ngoc Hung Nguyen, Kutluyıl Doğançay, Paul E. Berry, and Hai-Tan Tran

Task Sponsor

SRS MSTC, National Security and ISR Division

S&T Program

Chief of National Security and ISR Division
MSTC Leader SRS: Andrew Shaw
STC Leader S&P: Leigh Powis
STC Leader SMA: Brett Haywood
STC Leader MRS: Joe Fabrizio
Author: Ngoc Hung Nguyen (University of South Australia)
Author: Kutluyil Doğançay (University of South Australia)
Author: Paul E. Berry
Author: Hai-Tan Tran
Rocco Melino
Robert Young
Sandun Kodituwakku
Emma Heading
Si Tran Nguyen

<table>
<tr><td colspan="3">DEFENCE SCIENCE AND TECHNOLOGY GROUP
DOCUMENT CONTROL DATA</td><td colspan="2">1. DLM/CAVEAT (OF DOCUMENT)</td></tr>
<tr><td colspan="3">2. TITLE

Convex Relaxation Methods: A Review and Application to Sparse Radar Imaging of Rotating Targets</td><td colspan="2">3. SECURITY CLASSIFICATION (FOR UNCLASSIFIED LIMITED RELEASE USE (L) NEXT TO DOCUMENT CLASSIFICATION)

Document (U)
Title (U)
Abstract (U)</td></tr>
<tr><td colspan="3">4. AUTHORS

Ngoc Hung Nguyen, Kutluyıl Dogancay, Paul E. Berry, and Hai-Tan Tran</td><td colspan="2">5. CORPORATE AUTHOR

Defence Science and Technology Group
PO Box 1500
Edinburgh, South Australia 5111, Australia</td></tr>
<tr><td>6a. DST GROUP NUMBER

DST-Group–RR–0444</td><td colspan="2">6b. AR NUMBER

AR-016-971</td><td>6c. TYPE OF REPORT

Research Report</td><td>7. DOCUMENT DATE

September, 2017</td></tr>
<tr><td>8. OBJECTIVE ID</td><td colspan="2">9. TASK NUMBER

N/A</td><td colspan="2">10. TASK SPONSOR

N/A</td></tr>
<tr><td colspan="3">11. MSTC

Surveillance and Reconnaissance Systems</td><td colspan="2">12. STC

Signatures and Phenomenology</td></tr>
<tr><td colspan="3">13. DOWNGRADING/DELIMITING INSTRUCTIONS</td><td colspan="2">14. RELEASE AUTHORITY

Chief, National Security and ISR Division</td></tr>
<tr><td colspan="5">15. SECONDARY RELEASE STATEMENT OF THIS DOCUMENT

Approved for Public Release

OVERSEAS ENQUIRIES OUTSIDE STATED LIMITATIONS SHOULD BE REFERRED THROUGH DOCUMENT EXCHANGE, PO BOX 1500, EDINBURGH, SA 5111</td></tr>
<tr><td colspan="5">16. DELIBERATE ANNOUNCEMENT

No Limitations</td></tr>
<tr><td colspan="5">17. CITATION IN OTHER DOCUMENTS

No Limitations</td></tr>
<tr><td colspan="5">18. RESEARCH LIBRARY THESAURUS

Compressive Sensing, Radar Imaging, Non-Cooperative Target Recognition (NCTR)</td></tr>
<tr><td colspan="5">19. ABSTRACT

In this report we explore the use of sparse signal representation methods in the radar imaging problem of rotating targets and compare their results. The ultimate goal is to estimate the spatial locations and corresponding reflectivities of the scatterers constituting a target, based on a signal scattered from it. We pay particular attention to the so-called convex relaxation methods, which presumably can give the sparsest possible solutions and are computationally tractable while providing provable theoretical performance guarantees. We provide a comprehensive survey on various convex relaxation problem formulations known to date, as well as known computational algorithms for solving the optimization problems. By using extensive numerical simulations with simple rotating point targets, we show that, while many of these methods perform satisfactorily for ‘on-grid’ cases, performance for ‘off-grid’ cases is mostly unsatisfactory, warranting much further research before they can be efficiently applied to the inverse problem of radar imaging.</td></tr>
</table>